



Science Arts & Métiers (SAM)

is an open access repository that collects the work of Arts et Métiers Institute of Technology researchers and makes it freely available over the web where possible.

This is an author-deposited version published in: <https://sam.ensam.eu>
Handle ID: <http://hdl.handle.net/10985/24863>

To cite this version :

Shaolin LIU, Azita AHMADI-SENICHAULT, Cyril LEVET, Jean LACHAUD - Development and validation of a local thermal non-equilibrium model for high-temperature thermal energy storage in packed beds - Journal of Energy Storage - Vol. 78, p.109957 - 2024

Development and validation of a local thermal non-equilibrium model for high-temperature thermal energy storage in packed beds

Shaolin Liu^{a,b,*}, Azita Ahmadi-Senichault^{a,b}, Cyril Levet^{a,b} and Jean Lachaud^{b,c}

^aArts et Métiers Institute of Technology, 33400, Talence, France

^bI2M - Institute of Mechanical Engineering of Bordeaux: UMR CNRS 5295, University of Bordeaux, Arts et Métiers Institute of Technology, Hesam Université, Bordeaux INP, INRAE, 33400, Talence, France

^cUniv. Bordeaux, 33400, Talence, France

ARTICLE INFO

Keywords:

Local thermal non-equilibrium
Macroscopic numerical simulations
Packed bed storage
Numerical inverse analysis
Variable thermophysical properties

ABSTRACT

High-temperature thermal energy storage (TES) in packed beds is gaining interest for industrial energy recovery. The wide range of temperature distributions causes significant variations in thermophysical properties of the fluid and solid phases, leading to inaccuracies of classical TES models and heat transfer correlations. The objective of this work is to develop and validate a detailed but pragmatic model accounting for high-temperature effects. Based on a literature survey spanning over several communities interested in high-temperature porous media, we propose a generic local thermal non-equilibrium model for granulate porous media accounting for conservation of mass, momentum and energy (two-equation temperature model). The effective parameters needed to inform the model are the effective thermal conductivities of the different phases and the heat transfer coefficient. An experimental-numerical inverse analysis method is employed to determine these parameters. A dedicated experimental facility has been designed and built to study a model granulate made of glass bead of 16 mm diameter. Experiments are conducted using the Transient Single-Blow Technique (TSBT) by passing hot air (ranging from 293 K to 630 K) through cold particles at various mass flow rates, covering a Reynolds number range of 58 to 252. The new model was implemented in the Porous material Analysis Toolbox based on OpenFoam (PATO) used to compute the transient temperature fields. Two optimization algorithms were employed to determine the parameters by minimizing the error between experimental and simulated temperatures: a Latin Hypercube Sampling (LHS) method, and a local optimization method Adaptive nonlinear least-squares algorithm (NL2SOL). The results indicate that the value of heat transfer coefficient h_e in the two-equation model falls in the range of $1.0 \times 10^4 \sim 1.93 \times 10^4 \text{ W/(m}^3 \cdot \text{K)}$ under the given conditions. The axial dispersion gas thermal conductivity was found to be around 5.9 and 67.1 times higher than the gas thermal conductivity at Peclet numbers of around 55 and 165, respectively. Furthermore, two improved correlations of Nusselt number ($Nu = 2 + 1.54 Re(T)^{0.6} Pr(T)^{1/3}$) and of axial dispersion gas thermal conductivity ($k_{dis,||} = 0.00053 Re(T)^{2.21} Pr(T) \cdot k_g$) are proposed and validated for a range of Reynolds number from 58 to 252. The overall approach is therefore validated for the model granulate of the study, opening new perspectives towards more precise design and monitoring of high-temperature TES systems.

1. Introduction

Thermal energy storage (TES) is receiving increased attention for the development of energy recovery technologies such as concentrated solar power (CSP) [1–3], advanced adiabatic compressed air energy storage (AACAES) [2, 4, 5], and industrial waste heat recovery [6]. Amongst the major technologies (sensible, latent and chemical energy storage) [7–10], sensible heat storage is the most developed and used in the industry [1, 11, 12]. Most industrial sensible heat storage systems rely on packed beds that offer advantages such as a large heat transfer area, low cost, and a wide operating range (293 K to 1000 K) [2, 13].

To optimize the design of these systems, the coupled heat and mass transfer between the carrier fluid and the packed-bed material needs to be well understood and modeled. Many authors have contributed to this topic [1–3, 12–20]. Heat transfer in a packed bed can either be

studied under the assumption of local thermal equilibrium (LTE) or local thermal non-equilibrium (LTNE) [1]. These models are also referred to as one-equation and two-equation models, respectively. Pati et al. [21] reviewed the applicability of one- and two-equation models. The choice of model is influenced by parameters such as the gas-to-solid thermal diffusivity ratio (α_g/α_s), Reynolds number ($Re = \rho_g u d_{por}/\mu_g$), and Darcy number ($Da = K/d_{por}^2$). Specifically, when the Reynolds number is greater than 50 and the thermal diffusivity ratio between the gas and solid phases (α_g/α_s) is higher than 30 [22], the two-equation model is required. Schumann [14] was the first to propose a two-equation energy model - one for carrier fluid and one for the packed-bed material; however, the heat capacity of the fluid and the thermal conductivities of both phases were neglected, and the model was one-dimensional. Saez et al. [16] improved Schumann's one-dimensional model by including

*Corresponding author at: Arts et Métiers Institute of Technology, 33400, Talence, France.
E-mail address: shaolin.liu@u-bordeaux.fr (S. Liu).

heat capacity for the fluid and thermal conductivities and adding thermal dispersion in the

Nomenclature

Greek symbols

α	thermal diffusivity, $k/\rho c_p$, $\text{m}^2 \text{s}^{-1}$
β	Forchheimer coefficient, m^{-1}
ε_i	volume fraction of the i -phase
μ_g	dynamic viscosity of gas, $\text{kg m}^{-1} \text{s}^{-1}$
ρ_i	density of the i -phase, kg m^{-3}

Latin symbols

a	specific gas-solid surface area, m^{-1}
A_{sg}	area of the s-g interface contained in the averaging volume, V , m^2
\mathbf{b}_{ii}	vector field that maps $\nabla \langle T_i \rangle^i$ onto \bar{T}_i in LTNE model
Bi	Biot number
c_1, c_2, c_3	coefficients associated with thermal conductivity
$c_{p,i}$	heat capacity of the i -phase, $\text{J kg}^{-1} \text{K}^{-1}$
D_b	tube diameter, m
d_{por}	particle diameter, m
Da	Darcy number
f	coefficients associated with Nusselt number
h_s	interstitial heat transfer coefficient, $\text{W m}^{-2} \text{K}^{-1}$
h_v	volumetric heat transfer coefficient, $\text{W m}^{-3} \text{K}^{-1}$
\mathbf{I}	Identity tensor
\mathbf{k}_{dis}	dispersion term of the thermal conductivity, $\text{W m}^{-1} \text{K}^{-1}$
$\mathbf{k}_{i,eff}$	effective thermal conductivity tensor of the i -phase, $\text{W m}^{-1} \text{K}^{-1}$
$\mathbf{k}_{i,sta}$	static term of the thermal conductivity of the i phase, $\text{W m}^{-1} \text{K}^{-1}$
k_j	thermal conductivity of the i -phase, $\text{W m}^{-1} \text{K}^{-1}$
k_τ	tube thermal conductivity, $\text{W m}^{-1} \text{K}^{-1}$
$\mathbf{k}_{i,con}$	conductivity term of the thermal conductivity of the i phase, $\text{W m}^{-1} \text{K}^{-1}$
$\mathbf{k}_{i,tor}$	tortuosity term of the thermal conductivity of the i phase, $\text{W m}^{-1} \text{K}^{-1}$
\mathbf{K}	permeability tensor, m^2
L	tube length, m

M	gas molar mass, kg mol^{-1}
Nu	Nusselt number based on h_s
\mathbf{n}_{gs}	outwardly directed unit normal vector pointing from the gas phase toward the solid phase, $\mathbf{n}_{gs} = -\mathbf{n}_{sg}$
p	gas pressure, $\text{kg m}^{-1} \text{s}^{-2}$
$\langle p \rangle^g$	Intrinsic average pressure, $\text{kg m}^{-1} \text{s}^{-2}$
Pr	Prandtl number
qm	gas mass-flow rate, kg s^{-1}
R	gas constant, $\text{J K}^{-1} \text{mol}^{-1}$
R_b	tube radius, m
R_{iw}	tube radius with wall thickness, m
Re	Reynolds number based on the particle diameter
S	the relative error
s_i	scalar field used in LTNE model
T_{av}	average air temperature, K
$\langle T_i \rangle^i$	intrinsic phase average temperature in the i -phase, K
T_g	gas temperature, K
\mathbf{u}	Darcy velocity, $\varepsilon_g \langle \mathbf{v}_g \rangle^g$, m s^{-1}
u	magnitude of the Darcy velocity, m s^{-1}
\mathbf{v}_g	velocity of the gas phase, m s^{-1}
$\langle \mathbf{v}_g \rangle^g$	intrinsic phase average velocity of the gas, m s^{-1}
$\langle \mathbf{v}_g \rangle$	superficial average velocity, m s^{-1}
$\tilde{\mathbf{v}}_g$	the deviation of gas velocity, $\tilde{\mathbf{v}}_g = \mathbf{v}_g - \langle \mathbf{v}_g \rangle^g$, m s^{-1}
\mathbf{X}	Forchheimer tensor

Subscripts

\parallel	horizontal flow directions
\perp	transverse flow directions
atm	atmosphere
con	conductivity
dis	dispersion
g	gas
in	inlet
inf	ambient
num	numerical
s	solid
sta	static
t	tube

flow direction (increase in conductivity due to the gas flow). The thermophysical properties were assumed to be constant because the inlet gas temperature was at most 70°C. Hanchen et al. [12] applied the model proposed by Saez et al. to high-temperature conditions (527°C) but neglected the dispersion term and assumed constant gas properties. Zanganeh et al. [18, 19] proposed a more comprehensive model that considered the radiative term in the effective gas thermal conductivity and variable thermophysical properties for a packed bed of rocks in the temperature range of 20–650°C. Anderson et al. [3, 20] further validated the two-equation one-dimensional model with varying thermophysical properties for a packed bed of alumina particles at both low (120°C) and high (700°C) temperatures. Ma et al. [23] developed a transient two-equation two-dimensional model that fully considers thermal dispersion and changes in thermophysical properties, expanding on the existing literature. In these works, the carrier fluid density and velocity are considered constant, which is a correct approximation for incompressible fluids (water, molten nitrate salts, ...). Using air as the carrier fluid, non-uniform temperature distributions inside packed beds leads to non-uniform gas density and viscosity, affecting the velocity and pressure distributions. We aim to fill this gap by accounting for mass and momentum conservation, namely by including the volume-averaged conservation of mass and momentum (Darcy-Forchheimer's law) into the model. Such models have been employed since the 1960's for very high-temperature applications such as space-vehicle heat shields [24]. Also, in previous TES studies, the dimensionless numbers (Reynolds, Prandtl) used in the correlations were assumed to be constant. We would like to discuss this assumption when variations of velocity and thermophysical properties are not negligible. The two-equation energy model writes as follows [25, 26]:

$$\frac{\partial}{\partial t} (\varepsilon_g \rho_g c_{p,g} \langle T_g \rangle^g) = \nabla \cdot (\mathbf{k}_{g,\text{eff}} \cdot \nabla \langle T_g \rangle^g) + h_v (\langle T_g \rangle^g - \langle T_s \rangle^s) \quad (1)$$

$$\begin{aligned} \frac{\partial}{\partial t} (\varepsilon_g \rho_g c_{p,g} \langle T_g \rangle^g) + \nabla \cdot (\rho_g c_{p,g} \langle \mathbf{v}_g \rangle^g \langle T_g \rangle^g) &= \nabla \cdot (\mathbf{k}_{g,\text{eff}} \cdot \nabla \langle T_g \rangle^g) \\ &+ h_v (\langle T_g \rangle^g - \langle T_s \rangle^s) \end{aligned} \quad (2)$$

where the gas volume fraction ε_g is equal to the porosity of the packed bed, h_v is the volumetric heat transfer coefficient, $c_{p,i}$ and $\mathbf{k}_{i,\text{eff}}$ respectively denote the heat capacity and effective thermal conductivity tensor of the i phase, $\langle T_i \rangle^i$ and $\langle \mathbf{v}_i \rangle^i$ denote the intrinsic phase average temperature for the i -phase and the intrinsic gas average velocity. For the development of TES models, three effective properties need to be evaluated: h_v , $\mathbf{k}_{s,\text{eff}}$ and $\mathbf{k}_{g,\text{eff}}$.

The heat transfer coefficient and corresponding correlation can be determined either experimentally [13, 17, 27–32] or through pore-scale simulation in representative geometries [25, 33, 34]. The experimental methods include both steady state [28, 29, 31, 32] and transient regime [13, 30] approaches. With the steady state approach, particles within the packed beds are heated with a resistive heater. Compressed air, serving as the working fluid, extracts heat from these heated particles. After reaching steady-state, the temperatures of the gas flow at the inlet, outlet, within the packed bed, as well as the surface temperature of the particles are monitored. These measurements are used to estimate the

heat exchange and infer the heat transfer coefficient. In the transient method, cold particles are heated using hot gas. The time evolution of average inlet, outlet, and inside gas flow temperatures, and particle temperatures, are recorded. The local heat transfer coefficient is derived from analyzing the spatial and time evolution of air and particle temperatures. The progress in optimization algorithms and computer resources has allowed the general usage of inverse methods to infer the parameters with more accuracy. Concerning the pore-scale simulation method, the volume averaging theory [25] have been applied to periodic structures, such as arrays of cylinders, to obtain h_v . With the progress of the resolution of computed micro-tomography and computer resources, pore-scale simulations are becoming a realistic approach to determine h_v [35, 36]. Using these two methods, numerous correlations were obtained for the heat transfer coefficient h_v in packed-bed under diverse conditions. A summary of the most widely used correlations and of their validity ranges is proposed in Table 1. However, the influence of temperature variations on these correlations is not specified. Taking the Wakao correlation as an example, it is based on published experimental data in the range of $3 < Re < 10000$, mostly based on intermediate temperature conditions and without providing the temperature range of validity. Most simulation models for high-temperature storage systems used this correlation for temperatures up to 1173 K [2, 23, 37, 38]. At high temperatures, a wide temperature distribution can cause non-uniform gas density and viscosity inside the packed bed. These varying thermal physical properties affect Re , which in turn affects Nu in the Wakao correlation. Temperature-dependent parameters should replace constant parameters in such correlations; also the linear coefficients (1.1 in Wakao's correlation) should be validated or re-evaluated.

Concerning the effective gas and solid thermal conductivities, a large amount of theoretical work has been done by theoreticians and there is now a good agreement that they respectively write [25, 39, 40]

$$\mathbf{k}_{g,\text{eff}} = \varepsilon_g k_g \mathbf{I} + \frac{k_s}{V} \int_{A_{gs}} \mathbf{n}_{gs} \mathbf{b}_{gs} dA - \rho_g c_{p,g} \langle \hat{\mathbf{v}}_g \mathbf{b}_{gs} \rangle = \mathbf{k}_{g,\text{con}} + \mathbf{k}_{g,\text{tor}} + \mathbf{k}_{\text{dis}} \quad (3)$$

$$\mathbf{k}_{s,\text{eff}} = \varepsilon_s k_s \mathbf{I} + \frac{k_g}{V} \int_{A_{gs}} \mathbf{n}_{gs} \mathbf{b}_{gs} dA = \mathbf{k}_{s,\text{con}} + \mathbf{k}_{s,\text{tor}} \quad (4)$$

where k_i denotes the thermal conductivity of the i phase, V is a representative elementary volume of the porous medium, A_{gs} is the area of the g-s interface contained in the averaging volume, \mathbf{n}_{gs} is the outwardly directed unit normal vector pointing from the gas phase toward the solid phase, $\mathbf{n}_{gs} = -\mathbf{n}_{sg}$, $\mathbf{v}_g \cdot \langle \mathbf{v}_g \rangle^g$, and $\hat{\mathbf{v}}_g = \mathbf{v}_g - \langle \mathbf{v}_g \rangle^g$ are respectively the gas velocity within the pores, the intrinsic phase average velocity, and the deviation velocity. The closure variables \mathbf{b}_{ii} ($i = g, s$) are the vector fields that map $\nabla \langle T_i \rangle^i$ onto \hat{T}_i , where \hat{T}_i is the spatial deviation temperature in the i -phase, more precisely [25], $\hat{T}_g = \mathbf{b}_{gg} \cdot \nabla \langle T_g \rangle^g - s_g (\langle T_g \rangle^g - \langle T_s \rangle^s) + \dots$, $\hat{T}_s = \mathbf{b}_{ss} \cdot \nabla \langle T_s \rangle^s + s_s (\langle T_s \rangle^s - \langle T_g \rangle^g) + \dots$. Note that in these derivations the effective radiative conductivity may be added as a contribution the effective solid conductivity for optically thick media [41]; this hypothesis is verified for packed beds as the grain size is small compared to the system.

In many research works, regardless of the experimental conditions, simple expressions of $\mathbf{k}_{g,\text{eff}}$ and $\mathbf{k}_{s,\text{eff}}$ as a function of gas and solid phase conductivities and the porosity of the homogeneous and isotropic packed

Table 1

Empirical correlations for the heat transfer coefficient in packed beds.

Year	Investigators	Correlation	Range	Remarks
1952	W. Ranz [28]	$Nu = 2 + 1.8Re^{0.5}Pr^{1/3}$	$10 < Re/\varepsilon_g < 1000$ not mentioned for T	experimental method, steady state constant properties
1970	Galloway et al. [29]	$Nu = 2 + 1.354Re^{1/2}Pr^{1/3} + 0.0326RePr^{1/2}$	$Re/\varepsilon_g < 5000$ $T=310$ K	experimental method, steady state constant properties
1979	Wakao et al. [17]	$Nu = 2 + 1.1Re^{0.6}Pr^{1/3}$	$3 < Re < 10000$ not mentioned for T	analysis of experimental data from the literature
2012	Yang et al. [30]	$Nu = 2.1 + 0.465Re^{0.63}Pr^{1/3}$	$100 < Re/\varepsilon_g < 5000$ 298 K $< T < 358$ K	experimental method, transient constant properties
2016	Naghash et al. [31]	$Nu = (0.0012 \pm 0.00273)Re_{dh}^{(1.647 \pm 0.501)}Pr^{1/3}$ $Re_{dh} = Re/1000(2\varepsilon_g/3\varepsilon_s)d_{por}$	$40 < Re < 120$ 299 K $< T < 338$ K	experimental method, steady state variable properties
2022	Qu et al. [13]	$Nu = 0.345/\varepsilon_g \cdot (2 + 1.033(Re/\varepsilon_g)^{0.6}Pr^{1/3})$	$200 < Re/\varepsilon_g < 1000$ 283 K $< T < 345$ K	experimental method, transient constant properties
2023	this work	$Nu = 2 + 1.54Re(T)^{0.6}Pr(T)^{1/3}$	$58 < Re < 252$ 293 K $< T < 630$ K	experimental method, transient variable properties

beds have been considered [12, 20, 42, 43]. In Eq.3, $k_{g,eff}$ is composed of three parts: the conductivity term $k_{g,con}$ accounts for a simple average of the thermal conductivity, the tortuosity term $k_{g,tor}$ represent the tortuosity of the phase repartition and the dispersion term $k_{g,dis}$ accounts for gas flow effects. $k_{g,tor}$ and $k_{g,dis}$ could be numerically estimated by solving a closure problem on a periodic unit cell representative of the structure [25, 39]. $k_{g,tor}$ is often neglected since $k_{g,dis}$ dominates [39]. Wakao et al. [27] and DeGroot et al. [39] described $k_{g,dis}$ in the axial and radial directions (respectively horizontal and transverse flow directions) as different coefficients multiplied with Reynolds Re and Prandtl Pr numbers. In Eq.4, $k_{g,eff}$ consists of the conductivity of the solid $k_{s,con}$ corrected to account for its tortuosity $k_{s,tor}$ [44], whereas the closure variable b_{ss} which is a function of the gas velocity v_g [25] integrates dispersion effects. Therefore, for high temperatures, the best approach is to use the models of Eq.3 and 4 with temperature-dependent thermal conductivities k_g and k_s .

In this context, the purpose of this article is to propose a generic two-equation model coupled with mass and momentum conservation for high-temperature conditions and to determine the effective parameters needed to inform the model, namely, the thermal conductivities and the heat transfer coefficient. For this purpose, we have designed and built a laboratory-scale heat storage facility where the gas temperatures at the inlet, at the outlet and within the packed bed are monitored. Glass beads with a diameter of 16 mm were selected as the heat storage medium. In Section 2, the experimental setup and test procedure are presented. In section 3, we present a numerical inverse analysis method that we have developed to infer the intrinsic parameters and that consists of a detailed numerical model of the packed bed and an advanced multi-objective optimization algorithm. In section 4, the experimental results and the estimated values of the two-equation parameters are presented and new correlations accounting for high-temperature effects are proposed and compared with the literature. Conclusions and outlook are discussed in section 5.

2. Experimental facility

The main characteristics of gas/solid packed-bed TES described in the literature have been reviewed by Esence et al [1]. These encompass a mix of large-scale industrial systems [18, 19] and a majority of reduced-scale laboratory set-ups [13, 23, 30, 45, 46]. In studies conducted at the laboratory scale, the diameter ratios (tube diameter to particle size) range from 3 to 32, with gas flow rates varying between 0.035 to 3.23 m/s [1]. To minimize the effect of diameter ratios on the distribution of fluid velocity, it is recommended that diameter ratio remains greater than 10 [47]. In most cases, the velocity of the gases is of the order 0.3 m/s [13, 45, 46]. The experimental facility presented in the following section was designed in alignment with these characteristics. It is based on a method called the transient single-blow technique (TSBT) [1]. With this approach, hot gas is used to heat particles inside packed beds and the time evolution of the gas temperature is recorded at the inlet, at the outlet and also at different locations within the packed bed to bring robustness to the inverse analysis.

2.1. Experimental system and test procedure

A schematic drawing and photograph of the experimental setup that we have developed and an enlarged view of the test section, where thermocouple positions are shown, are displayed in Fig.1. The setup consists of a hot air blower (BAK Thermoplastic) to supply and heat air, an insulated test section made of an iron tube and two metallic grids to maintain the particles, a differential pressure transmitter (EMERSON FISHER ROSEMOUNT) to measure pressure drop and a thermo-anemometer (VT 110-2014 THERMO-ANEMOMETER) to measure the gas velocity. The iron tube has dimensions of 940 mm in length, 194 mm in inner diameter, and a thickness of 3 mm. These dimensions are suitable to study glass beads with a diameter of 16 mm, while respecting the diameter aspect ratio of at least 10, recalled in the introduction.

In the experiment, the first step is to set the flow rate of the inlet gas. This parameter is controlled by the air blower and measured using the thermo-anemometer. The maximum flow rate is 800 liters/min,

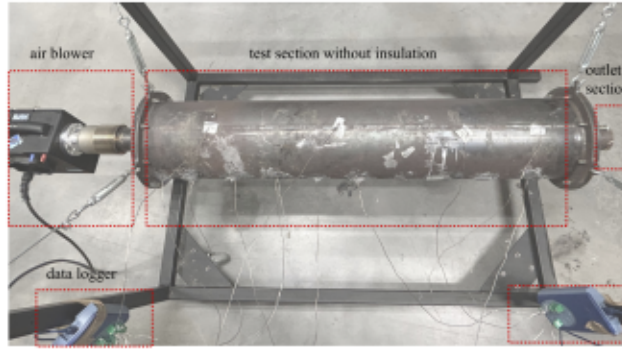
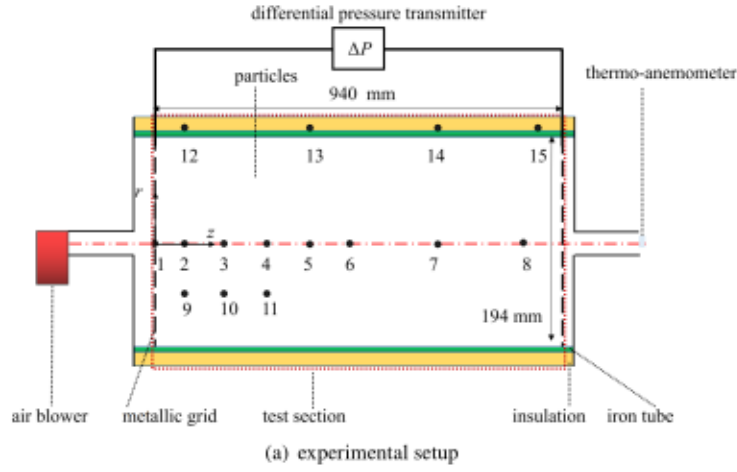


Figure 1: Schematic diagram and photograph of the experimental system and enlarged view of the test section showing the thermocouple identification numbers.

equivalent to a mass flow rate of 1.6×10^{-2} kg/s. The maximum Darcy velocity u (also known as superficial gas velocity, $u = qm/(\rho_g \pi R_b^2)$) reaches 0.451 m/s at room temperature (293 K), where ρ_g is the gas density of 1.2 kg/s and R_b is the radius of the tube at 0.097 m. Once the inlet air mass flow rate is determined at room temperature, the next step involves setting the heating power, which is also controlled by the air blower. To ensure data reproducibility, we repeated each experiment following a consistent procedure. After an initial experiment, with a two-day cooldown period to return particles to room temperature, subsequent runs exhibited only minor temperature differences (1-2 °C) initially due to the room temperature. After 15 minutes of heating, the temperature differences remained minimal, within 0.3 °C, confirming data reliability across trials.

The black points in Fig. 1 indicate the positions of the thermocouples (type K, 2 mm sheath diameter). Temperature measurements are taken at various locations: the inlet gas temperature (1) at $z=0$ mm, $r=0$ mm; the gas temperature inside the test section at seven central axis locations (from 2 to 8) at $z=50, 150, 250, 350, 450, 650,$ and 850 mm, $r=0$ mm; and three radial locations (from 9 to 11) at $z=50, 150,$ and 250 mm, $r=45$ mm. The tube surface temperature is also measured at four axis locations (from 12 to 15) at $x=50, 350, 650,$ and 900 mm, $z=100$ mm.

To ensure accurate gas temperature measurement, the thermocouple is securely fixed in the gap between the glass beads using ST-1000 thermal glue, as shown in Fig. 2. The thermal glue is capable of withstanding temperatures up to 950°C.

The thermocouples are connected to two display data loggers (Pico Technology TC-08) that record the temperature with a time step of 1.0 s. Experimental variations in the inlet air mass-flow rate and heating power were performed to verify the model's suitability for different Reynolds numbers (Re). The test section dimensions and the architectural properties of particles are listed in Table 2. The gas volume fraction (porosity, ϵ_g) in Table 2 is calculated using the Muller correlation [47, 48] as shown in Eq. 5. The permeability and Forchheimer coefficient are calculated using the Ergun equation, as shown in Eq. 6 [1], where these two parameters are treated as scalars. These defined parameters will be used in the subsequent modeling section. Ergun equation is validated for modeling pressure variations in the experiments, as explained in Appendix A.

$$\epsilon_g = 0.365 + 0.22/(D_b/d_{par}) \quad (5)$$

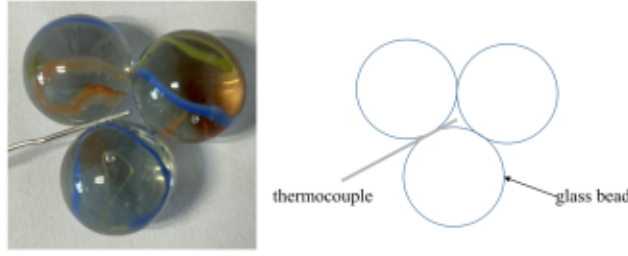


Figure 2: A schematic of the thermocouple position.

Table 2

Dimension and structural properties of the packed bed and glass beds.

Test section dimensions diameter D_b \times length L (mm)	Porosity ϵ_g	Particle diameter d_{par} (mm)	Particle density ρ_s (kg m ⁻³)	Permeability K (m ²)	Forchheimer coefficient β (m ⁻¹)
194 \times 940	0.383	16	2500	2.52×10^{-7}	1201.18

Table 3

The uncertainty analysis in the experimental measurements.

	Range	Uncertainty
Temperature sensor (Pico Technology)	-270°C to +1820°C	$\pm 0.2\%$ of the reading
K-type thermocouple	-100°C to + 800°C	$\pm 0.5 \%$
Thermo-anemometer	0.15 to 30 m/s	$\pm 3 \%$ of the reading
Temperature measurement in the tube (due to the position of the thermocouple)	293 K to 630 K	1.19 % of the reading

$$K = \frac{d_{par}^2 \epsilon_g^3}{150 \epsilon_g^2}, \quad \beta = \frac{1.75 \epsilon_g}{d_{par} \epsilon_g^3} \quad (6)$$

2.2. Experimental uncertainty analysis

Experimental uncertainties can be categorized into two types: direct measurement errors resulting from the experimental device, and errors arising from the measurement process itself. In this work, the ranges and uncertainties associated with the experimental devices are presented in Table 3. Errors from the temperature measurement process are chiefly due to the positioning of the thermocouples in the tube. The thermocouples are fixed in the gap between the glass beads, which are positioned with a tolerance of ± 10 mm. The uncertainty in temperature measurement within the tube, attributed to the thermocouple positioning, is determined through repeated experiments, resulting in an uncertainty value of 1.19%.

3. Numerical inverse analysis method

To tackle the complexity of the problem, numerical inverse analysis was employed to estimate the desired quantities. Firstly, we present the model describing fluid flow and heat transfer within the test section. Secondly, we detail the multi-objective optimization algorithm used to infer the effective parameters.

3.1. Numerical model

To facilitate parameter estimation, we model the entire test section as shown in Fig.1 (b). The corresponding numerical model, presented in Fig.3, represents a two-dimensional axisymmetric geometry. The model consists of two regions, namely the packed bed (porous sample) and the tube (iron tube).

3.1.1. Mathematical model and numerical implementation

In the packed bed region, we consider the two-equation model (Eq.1 and 2) for energy conservation. For the tube region, transient heat conduction is considered (energy conservation in a solid). The Reynolds number based on the particle diameter (d_{par}) is defined as $Re = \rho_g u d_{par} / \mu_g$. Throughout the entire experimental process, the minimum value of Re is 18.34 (corresponding to $T_g=630$ K, $\rho_g=0.563$ kg/m³, $u=0.067$ m/s, $\mu_g=3.29e-05$ kg/(m · s)), and the maximum value of Re is 453.36 (corresponding to $T_g=293$ K, $\rho_g=1.2$ kg/m³, $u=0.451$ m/s, $\mu_g=1.91e-05$ kg/(m · s)). Considering the range of applicability of the Forchheimer law inside a packed bed, which typically lies between 5 [49] and 500 to 600 [50], the average gas velocity is determined by solving the Forchheimer law. The two regions are coupled by ensuring the conservation of heat fluxes at their interfaces. The mass and energy conservation equations for the two-equation model in the packed bed

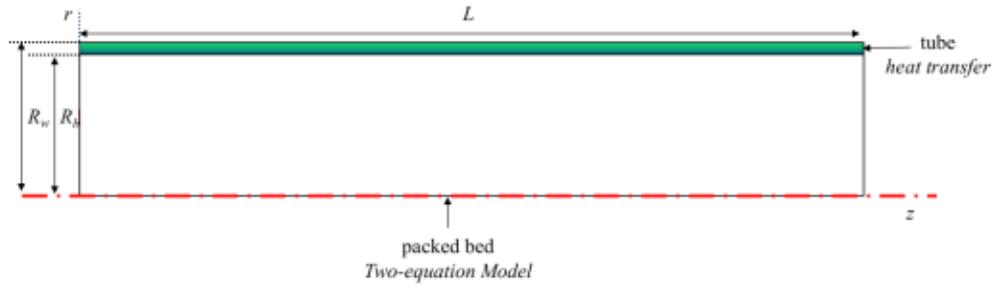


Figure 3: Two-dimensional axisymmetric numerical model of the test section.

region and the energy equation in the tube region write,

$$\begin{cases} \frac{\partial}{\partial t} \left(\epsilon_g \frac{M \langle p \rangle^g}{R \langle T_g \rangle^g} \right) + \nabla \cdot \left(- \frac{M \langle p \rangle^g \mathbf{K} \mathbf{X}}{R \langle T_g \rangle^g} \cdot \nabla \langle p \rangle^g \right) = 0 & \text{(Mass equation)} \\ \frac{\partial}{\partial t} (\epsilon_g \rho_g c_{p,g} \langle T_g \rangle^g) = \nabla \cdot (\mathbf{k}_{g,eff} \cdot \nabla \langle T_g \rangle^g) + h_c (\langle T_g \rangle^g - \langle T_s \rangle^s) & \text{(Energy equation)} \\ \frac{\partial}{\partial t} (\epsilon_g \rho_g c_{p,g} \langle T_g \rangle^g) + \nabla \cdot (\rho_g c_{p,g} \langle \mathbf{v}_g \rangle^g \langle T_g \rangle^g) = \nabla \cdot (\mathbf{k}_{g,eff} \cdot \nabla \langle T_g \rangle^g) \\ + h_c (\langle T_g \rangle^g - \langle T_s \rangle^s) & \text{(Energy equation)} \\ \rho_t c_{p,t} \frac{\partial T_t}{\partial t} = \nabla \cdot (k_t \cdot \nabla T_t) & \text{(Energy equation)} \end{cases} \quad (7)$$

where $\langle p \rangle^g$ is the intrinsic average pressure, the mass equation is derived from the perfect gas law (Eq. 8), gas mass conservation (Eq. 9) [24], and the Forchheimer equation (Eq. 10). The Forchheimer tensor, represented as \mathbf{X} , is introduced to simplify the computation process [51].

$$\rho_g = \frac{M \langle p \rangle^g}{R \langle T_g \rangle^g} \quad (8)$$

$$\partial_t (\epsilon_g \rho_g) + \nabla \cdot (-\epsilon_g \rho_g \langle \mathbf{v}_g \rangle^g) = 0 \quad (9)$$

$$\langle \mathbf{v}_g \rangle^g = - \frac{1}{\epsilon_g} (\mathbf{K} \mathbf{X}) \cdot \nabla \langle p \rangle^g, \quad X_{ij} = \frac{1}{\mu_g K_{ij} + \beta_{ij} \rho_g |\langle \mathbf{v}_g \rangle^g|} \quad (10)$$

It should be noted that glass beds exhibit significant opacity at a wavelength of 4.9 μm , which coincides with the peak intensity wavelength at 700 K. For 5 mm glass beds, radiation contributes to nearly 0% of the total heat transfer at temperatures below 700 K, while it increases to 50% at 1000 K [52]. Therefore, it is reasonable to neglect radiation heat transfer effects when the temperature is below 700 K. The initial and boundary conditions for the systems of Eq.7 are described in detail in Table 4. In the packed bed region, T_g and T_s represent the gas and solid temperatures, respectively, while T_t represents the temperature in the tube region. The thermal conductivity of the tube is denoted as k_t . For simplicity, we use T_g , T_s , and p to represent the average gas temperature $\langle T_g \rangle^g$, average solid temperature $\langle T_s \rangle^s$, and average pressure $\langle p \rangle^g$, respectively. The gas temperature T_g at the inlet side is determined from the experimental study. Numerically, we imposed the inlet mass flux using a pressure gradient inlet boundary condition based on Darcy-Forchheimer's law projected on the inlet patch normal \mathbf{n} . The expression of the inlet pressure gradient imposed is provided in Table 4. In the tube region, the wall surface temperature T_t is measured throughout the experimental period. At the interface between the packed bed and the tube, the condition of $T_g = T_t$, $k_{g,eff} \frac{\partial T_g}{\partial r} = k_t \frac{\partial T_t}{\partial r}$ were applied for

the gas phase. By implementing this boundary condition, which implies that the gas temperature T_g and the tube temperature T_t are equal at this interface, it also guarantees that the heat flux entering one region on one side of the interphase matches the heat flux leaving the other region on the opposite side of the domain. At the packed bed-tube interface, the condition of $\partial T_s / \partial r = 0$ was used for the solid phase. This boundary condition is in line with the practical situations and finds support in the existing literature [38]. A linear part variation of T_t within each interval is assumed in line with the findings reported by Cascetta et al. [38] in a similar experimental setup. The temperatures at the four measuring points (from 12 to 15) shown in Fig. 1 (b) are expressed as follows

$$\begin{cases} T_t = T_{12} + (T_{12} - T_{13}) / (z_{13} - z_{12}) \cdot (z_{12} - z) & 0 < z < z_{13} \\ T_t = T_{13} + (T_{13} - T_{14}) / (z_{14} - z_{13}) \cdot (z_{13} - z) & z_{13} \leq z < z_{14} \\ T_t = T_{14} + (T_{14} - T_{15}) / (z_{15} - z_{14}) \cdot (z_{14} - z) & z_{14} \leq z < L \end{cases} \quad (11)$$

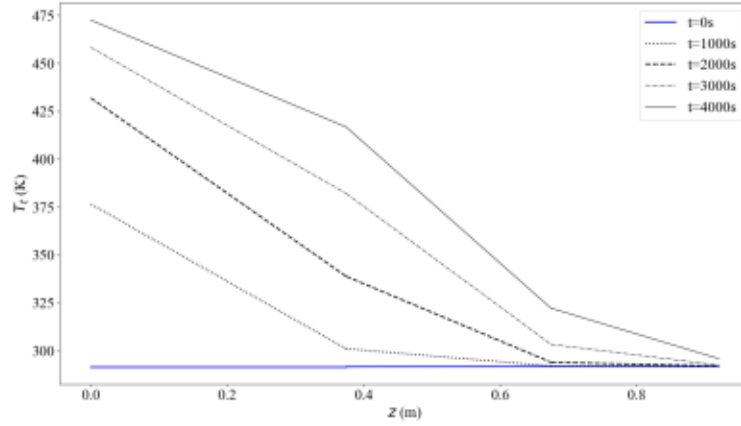
Fig.4 shows the temperature distribution of T_t on the wall surface, which is calculated using Eq.11. In this case, the inlet gas temperature T_g gradually increases from 292 K to 530K, and the inlet mass-flow rate qm is chosen as 5.97×10^{-3} kg/s. As shown in Fig.4, T_t exhibits a linear variation along the z-axis within each of the three zones as a function of time and space.

The numerical model was implemented in the Porous material Analysis Toolbox based on OpenFOAM (PATO) [53], using a finite volume method. A multi-block approach was employed, where different sets of equations were solved in each region at each time step, incorporating appropriate boundary conditions derived from the energy balances at the interfaces. A wedge-mesh for axisymmetrical simulations was generated using the *blockMesh* application of OpenFOAM. The mesh is refined at the near-tube region as shown in Fig.5. In the packed bed region, the pressure equation was solved semi-implicitly using first-order schemes in time (Euler) and space (Gauss linear). Similarly, the energy equations were solved with an implicit treatment of the temperature terms and an explicit treatment of other quantities. In the tube region, only the energy equation needed to be solved, with the temperature terms treated implicitly and other quantities treated explicitly. The equations are solved in series, with appropriate mesh refinement and time steps to guarantee that the order of convergence is reached.

Table 4

Initial and boundary conditions of the two-equation model.

Region	Initial conditions		Boundary conditions		
packed bed	$T_g = T_0$	inlet $T_g = T_1, \frac{\partial T_g}{\partial z} = 0$	packed bed-tube interface $\frac{\partial T_g}{\partial r} = 0, T_g = T_t, k_{g,eff} \frac{\partial T_g}{\partial r} = k_t \frac{\partial T_t}{\partial r}$	outlet $\frac{\partial T_g}{\partial z} = 0, \frac{\partial T_s}{\partial z} = 0$	
	$T_s = T_0$	$\partial_w p = -\left(\frac{\rho_g}{k_{nn}} + \rho_g \beta \cdot \mathbf{n} \cdot \mathbf{n} \epsilon \mathbf{v}_g \right) (\epsilon \mathbf{v}_g \cdot \mathbf{n}) + \rho_g g$	$\frac{\partial p}{\partial r} = 0$	$p = p_{atm}$	
tube	$T_t = T_0$	inlet $\frac{\partial T_t}{\partial z} = 0$	tube-packed bed interface $k_t \frac{\partial T_t}{\partial r} = k_{g,eff} \frac{\partial T_g}{\partial r}$	top T_t is a function of wall surface temperature	outlet $\frac{\partial T_t}{\partial z} = 0$

**Figure 4:** Wall surface temperatures input in the simulation ($qm=5.97 \times 10^{-3}$ kg/s).

3.1.2. Physical properties of air and glass

This model takes into account the temperature-dependent properties of both the gas and solid phases. The density of air, ρ_g , is calculated using the perfect gas law, while the values for the heat capacity, $c_{p,g}$, dynamic viscosity, μ_g , and thermal conductivity, k_g , are obtained from the NASA-9 database [54]. The density of glass, ρ_s , is assumed to be constant at 2500 kg/m³, while the heat capacity, $c_{p,s}$, and thermal conductivity, k_s , are determined by fitting experimental data from Pertermann et al. [55] as described in Eq.12.

$$\begin{cases} k_s = 0.59206 + 0.00062T_s + 1.0013 \times 10^{-6}T_s^2 - 2.778 \times 10^{-10}T_s^3 \\ c_{p,s} = 316.506 + 2.0745T_s - 0.00199T_s^2 + 7.4369 \times 10^{-7}T_s^3 \end{cases} \quad (12)$$

Table 5 provides the temperature-dependent properties for both the gas and solid phases used in the numerical model. The values for each property are given at specific temperatures, and linear interpolation is employed between two adjacent values to estimate the property at intermediate temperatures.

As discussed in Section 1, the determination of three unknown effective parameters, namely the effective solid thermal conductivity $k_{s,eff}$, effective gas thermal conductivity $k_{g,eff}$, and volumetric heat transfer coefficient h_v , is required in the two-equation model (Eq.1 and 2). To facilitate the optimization algorithm, several dimensionless

coefficients, including c_1 , c_2 , c_3 , and f , are defined as presented in Eq.13.

$$\begin{cases} k_{s,eff} = k_{s,con} + k_{s,tor} = c_1 \cdot k_s I \\ k_{g,eff,||} = k_{g,con} + k_{g,tor,||} + k_{dis,||} = \epsilon_g k_g + 0 + c_2 \cdot Re \cdot Pr \cdot k_g \\ \quad = \epsilon_g k_g + c_2 \cdot d_{par} \cdot \epsilon_g \cdot |\langle v_g \rangle^g| \cdot \rho_g \cdot c_{p,g} \\ k_{g,eff,\perp} = k_{g,con} + k_{g,tor,\perp} + k_{dis,\perp} = \epsilon_g k_g + 0 + c_3 \cdot Re \cdot Pr \cdot k_g \\ \quad = \epsilon_g k_g + c_3 \cdot d_{par} \cdot \epsilon_g \cdot |\langle v_g \rangle^g| \cdot \rho_g \cdot c_{p,g} \\ h_v = (6\epsilon_s/d_{par}) \cdot (2 + f Re^{0.6} Pr^{1/3}) k_g / d_{par} \end{cases} \quad (13)$$

The effective gas thermal conductivity, $k_{g,eff}$, is influenced by the tortuosity and dispersion terms, which have different values in the horizontal (||) and transverse (\perp) flow directions [1, 27]. Typically, the tortuosity term is neglected compared to the dispersion term [39]. The relationship between k_{dis} and the thermal properties of the gas is modeled similarly to the formulation proposed by Wakao et al. [27]. The volumetric heat transfer coefficient, h_v , is modeled using the functional form proposed by Wakao et al. [17]. The parameters c_1 , c_2 , c_3 , and f will be optimized as described in section 3.2.

3.2. Optimization process

A numerical inverse analysis method was employed to infer the intrinsic parameters from experimental measurements in order to minimize errors between measured and predicted data. We have eleven data sequences $\{T1^i\}_{i=0}^n, \{T2^i\}_{i=0}^n, \{T3^i\}_{i=0}^n, \{T4^i\}_{i=0}^n, \{T5^i\}_{i=0}^n, \{T6^i\}_{i=0}^n,$

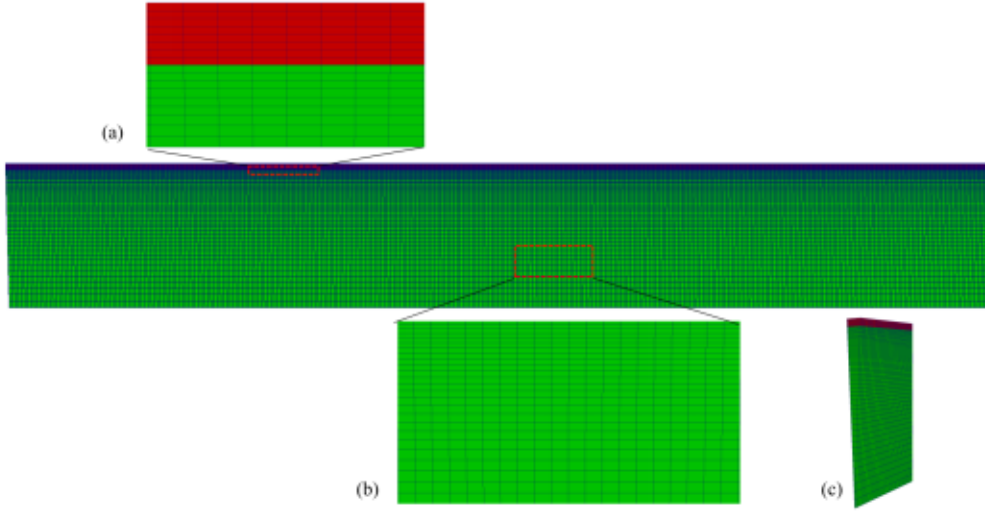


Figure 5: PATO multi-block mesh. (a) Zoom at the interface. (b) Zoom at the packed bed region (c) Side view of wedge-mesh.

Table 5

Thermal properties of gas and solid as a function of temperature.

$T(K)$	gas			solid	
	$c_{p,g}$ ($J kg^{-1} K^{-1}$)	μ_g ($kg m^{-1} s^{-1}$)	k_g ($W m^{-1} K^{-1}$)	$c_{p,s}$ ($J kg^{-1} K^{-1}$)	k_s ($W m^{-1} K^{-1}$)
273	1009.8	1.853e-05	0.02713	749.54	0.831
290	1010.4	1.909e-05	0.02798	768.75	0.850
340	1013	2.105e-05	0.03091	820.82	0.909
390	1017.5	2.306e-05	0.03401	866.73	0.971
440	1023.9	2.507e-05	0.03719	907.02	1.035
490	1032	2.710e-05	0.04049	942.27	1.105
540	1041.5	2.9135e-05	0.044	973.03	1.177
590	1055.7	3.1198e-05	0.0476	1000.48	1.249
640	1067.6	3.2993e-05	0.0508	1024.03	1.326
690	1079.8	3.4712e-05	0.0541	1044.78	1.405
740	1092.06	3.6432e-05	0.0574	1063.27	1.486

$\{T7^i\}_{i=0}^n, \{T8^i\}_{i=0}^n, \{T9^i\}_{i=0}^n, \{T10^i\}_{i=0}^n, \{T11^i\}_{i=0}^n$, which correspond to the measured gas temperatures collected at each time step indicated by the index i (see Fig.1 (b)). The transient inlet gas temperature data $T1$ is fitted into a second-order polynomial using least squares and is used as a boundary condition. The objective function S for the optimization processes is defined as the average of the root mean squared relative error between the measured and predicted temperatures at the ten positions mentioned ($T2, T3, T4, T5, T6, T7, T8, T9, T10, T11$):

$$S = \frac{1}{10} \left(\sqrt{\frac{1}{n} \sum_{i=1}^n \left(\frac{T2_{num}^i - T2^i}{T2^i} \right)^2} + \sqrt{\frac{1}{n} \sum_{i=1}^n \left(\frac{T3_{num}^i - T3^i}{T3^i} \right)^2} + \dots + \sqrt{\frac{1}{n} \sum_{i=1}^n \left(\frac{T11_{num}^i - T11^i}{T11^i} \right)^2} \right) \quad (14)$$

The minimization of S was performed using the Design Analysis Kit for Optimization and Terascale Applications (Dakota) [56]. The optimization process involved a combination of the Latin hypercube sampling (LHS) method [57] for sensitivity analysis and the Adaptive nonlinear least-squares algorithm (NL2SOL) [58] for local optimization.

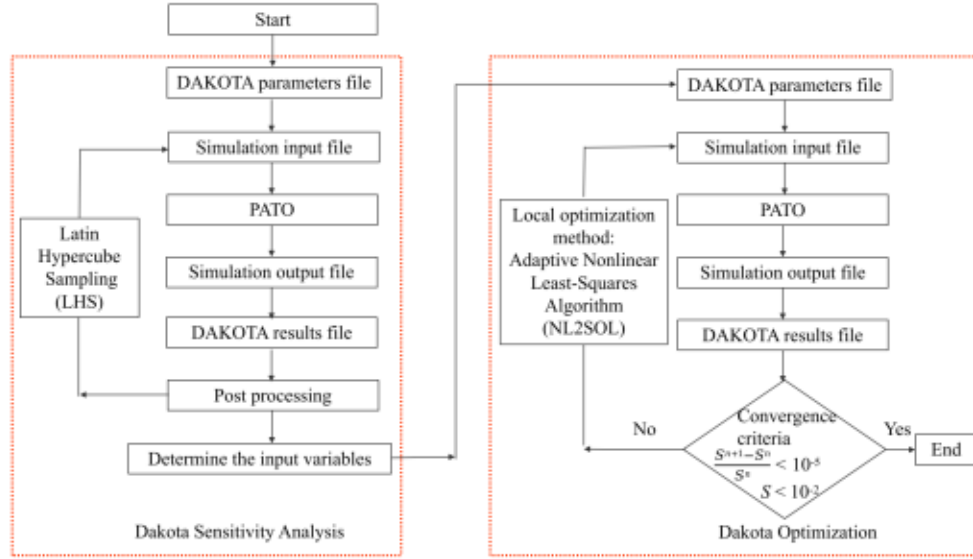


Figure 6: The steps of sensitivity analysis and optimization process.

LHS was employed initially for sensitivity analysis to identify the most important input variables and their interactions. This stratified sampling technique divides the range of each uncertain variable into N_s segments of equal probability, resulting in a more accurate estimate of the mean value compared to random sampling. The next step involved local optimization using NL2SOL. This algorithm utilizes a quasi-Newton update to quickly converge to an optimal solution. By employing a simplification scheme to approximate the Hessian, NL2SOL achieves faster convergence compared to global optimization methods when performing least square calculations. An overview of this optimization strategy is presented in Fig.6, which will be further explained in the subsequent section through examples of applications to two-equation model optimizations.

4. Results and discussions

In this section, we present the results of both measured and predicted temperatures. In the first subsection, we determine the volumetric heat transfer coefficient h_v , the effective solid thermal conductivity $k_{s,eff}$, and the effective gas thermal conductivity $k_{g,eff}$ used in the two-equation model. Additionally, we provide the predicted fields of gas properties, pressure, velocity, temperature, and volumetric heat transfer coefficient using the two-equation model. In the second subsection, we focus on evaluating the validity of the obtained effective parameters.

Fig.7 presents a comparison of the measured and predicted results for four mass-flow rates. The relative errors, represented by the objective function S , are below 10^{-2} for all cases. Detailed data can be found in Table 7. A discussion of these results can be found in the following subsections. The measured results are represented by dots, while the predicted results obtained by solving the two-equation model are shown as solid and dashed lines. The recorded inlet gas temperature (T_1), and gas temperature at ten locations (T_2 to T_{11}) are plotted as a function of

time. The presented temperature data represents the subset that was used in the optimization process. In the predicted results, gas temperatures at seven points along the central axis ($T_{2,num}$ to $T_{8,num}$) are shown as solid lines, and the other three points ($T_{9,num}$ to $T_{11,num}$) with dashed lines.

The experimental parameters at room temperature are shown in Table 6. In the first case, the inlet gas temperature gradually increases from room temperature to 630 K, the inlet gas mass-flow rate is 3.65×10^{-3} kg/s, and the superficial gas velocity at room temperature is 0.10 m/s. The Reynolds number at room temperature is 101. The fluctuation in the inlet gas temperature might be caused by the tolerance of the thermocouple. Error bars indicate the uncertainty in the measured temperatures, as described in Section 2, where it was noted that the error due to the uncertain position of the thermocouples was estimated to be 1.19%. The major parameters that can affect the predicted temperatures are $k_{s,eff}$, $k_{g,eff}$, and h_v . In the following, we present the procedure for determining these parameters.

4.1. Optimization and numerical results

In this subsection, we focus on determining the three effective parameters used in the two-equation model. Next, we present the numerical results, including the pressure, velocity, and temperature fields throughout the whole test section.

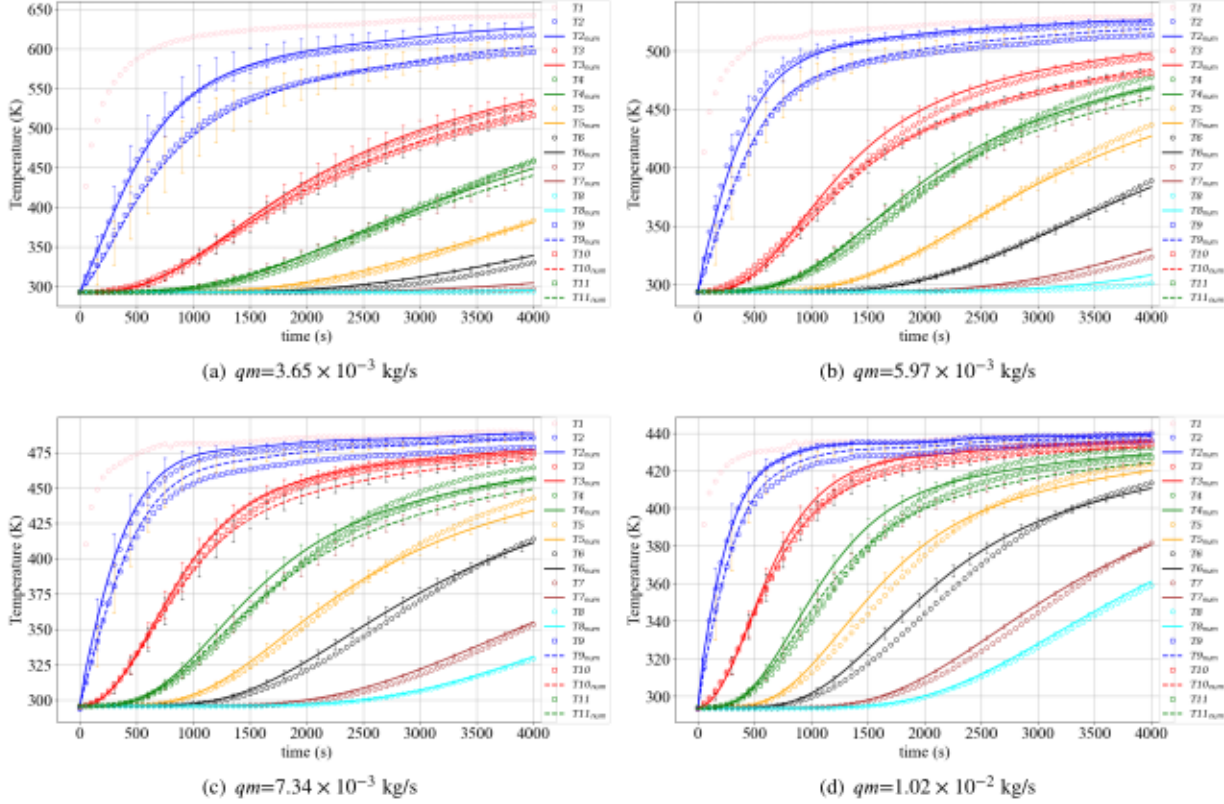
4.1.1. Determination of three effective parameters used in the two-equation model

As discussed in Subsection 3.2, the estimation of these effective parameters involves two modules: sensitivity analysis and the optimization process. To begin, a sensitivity analysis is performed to understand the relationship between the output result (S) and the input variables (f , c_1 , c_2 , c_3). In this analysis, we use a high mass-flow rate case ($qm = 1.02 \times 10^{-2}$ kg/s) as an example to demonstrate the sensitivity

Table 6

Experimental parameters at room temperature.

case	inlet gas temperature T_1 (K)	mass-flow rate qm (kg s^{-1})	magnitude Darcy velocity u (m s^{-1})	Reynolds number Re
case1	630	3.65×10^{-3}	0.10	101
case2	530	5.97×10^{-3}	0.16	165
case3	490	7.34×10^{-3}	0.20	203
case4	440	1.02×10^{-2}	0.28	282

**Figure 7:** Comparison of predicted and measured temperatures with different mass-flow rates.

analysis and optimization method. Additional case results are presented in Appendix B.

During the sensitivity analysis, it is important to select appropriate minimum and maximum values for the parameters to be optimized. To determine these values, we refer to the correlations provided by Esence et al. [1] for packed beds. Based on their work, the coefficients f , c_1 , c_2 , and c_3 are estimated to be 1.1, 0.617, 0.1, and 0.001, respectively, for Reynolds numbers less than 8000. In order to assess the sensitivity of the model to these parameters, we employ the Latin hypercube sampling (LHS) method. The ranges for f , c_1 , c_2 , and c_3 are defined as follows: f ranges from 0.7 to 2.5, c_1 ranges from 0.4 to 1.8, c_2 ranges from 0.01 to 0.5, and c_3 ranges from 0 to 0.01. The LHS method ensures that the input

variables are evenly distributed within these minimum and maximum boundaries.

Fig.8 presents a typical result of the sensitivity analysis. The red line represents the strength and direction of the relationship between the independent variables (f , c_1 , c_2 , and c_3) and the dependent variable (S). The slope of the red line corresponds to the partial correlation coefficient (PCC), which quantifies the linear relationship between two variables (x : f or c_1 or c_2) and y (S) while accounting for the influence of one or more additional variables [56, 59]. The PCC is calculated using the following

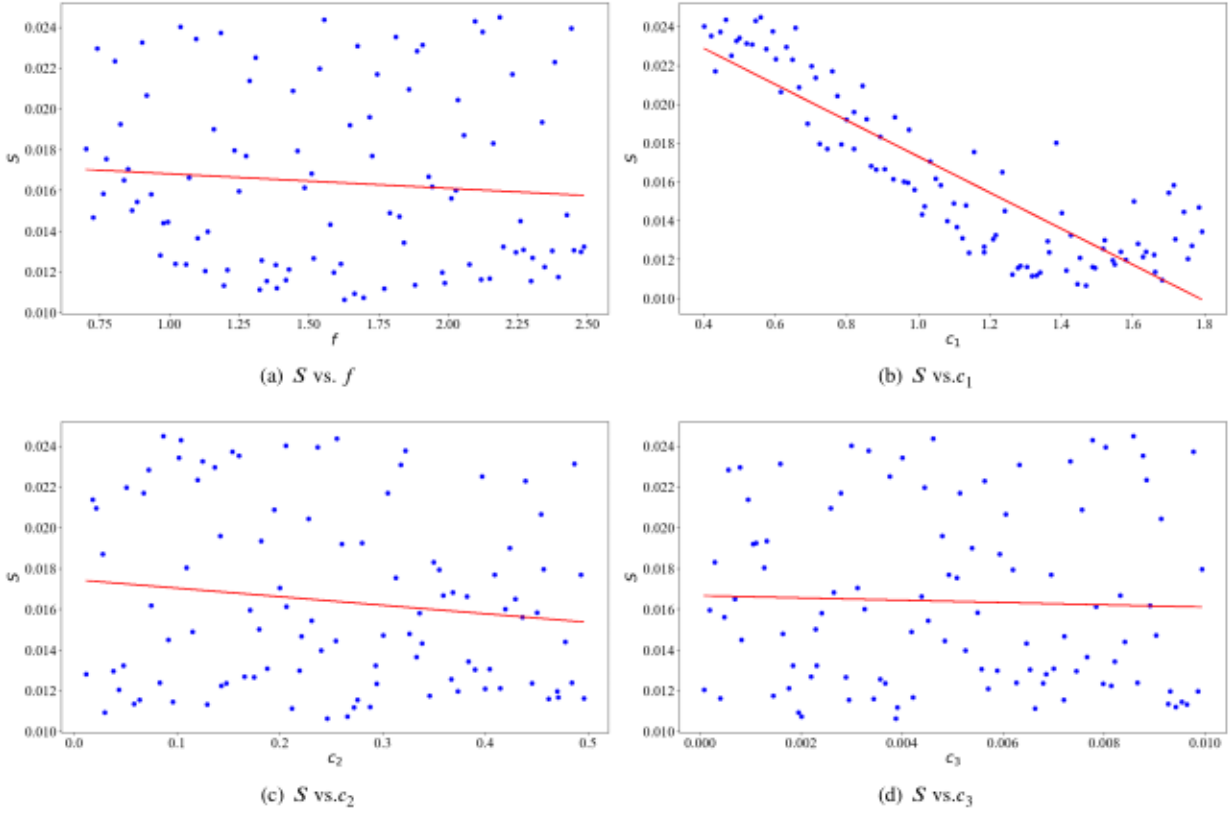


Figure 8: Sensitivity analysis of the error S to input parameters (f , c_1 , c_2 , c_3), $qm = 1.02 \times 10^{-2}$ kg/s.

formula:

$$\text{PCC}(x, y) = \frac{\sum_i (x_i - \bar{x})(y_i - \bar{y})}{\sqrt{\sum_i (x_i - \bar{x})^2 \sum_i (y_i - \bar{y})^2}} \quad (15)$$

$$\hat{x}_i = c_0 + \sum_{p=1, p \neq i}^n c_p x_p, \quad \hat{y} = b_0 + \sum_{p=1, p \neq i}^n b_p x_p$$

where \bar{x} and \bar{y} represent the mean values of x and y . x_i and y_i denote individual values (samples) of the two variables. The regression equations \hat{x}_i and \hat{y} are defined by real number coefficients b and c , and x_p represents the other variables except for x_i . PCC can help to identify the variables that have the most significant impact on the output results and should be prioritized in the optimization process. In this case, the PCC values between the input variables (f , c_1 , c_2 , and c_3) and the output variable (S) are -0.12, -0.87, -0.22, and -0.04, respectively. A coefficient closer to ± 1 indicates a strong correlation between the input and output variables. The results show a very low correlation between c_3 and S . Therefore, we shifted our focus to investigating the effects of the other three variables, f , c_1 , and c_2 on the output result S .

During the optimization process, the boundary values for the three variables (f , c_1 , c_2) were set the same as in the sensitivity analysis: f ranging from 0.7 to 2.5, c_1 ranging from 0.4 to 1.8, and c_2 ranging from 0.01 to 0.5. Convergence ($S < 0.01$) was reached after 50 iterations of the local optimization algorithm NL2SOL. Fig.9 shows the influence of

the three variables (f , c_1 , c_2) on the error S . The size of the points in Fig.9 (a) represents the value of S , while the grey scale indicates the value of f . As shown in Fig.9 (a), when S is below 0.01, the values of c_1 are concentrated around 1.29 and c_2 are concentrated around 0.42, while the values of f range from 1.0 to 2.0. To further analyze the behavior of the error when varying f , we set c_1 to 1.29 and c_2 to 0.42 and only varied f as the input parameter. As shown in Fig. 9 (b), S displays a decreasing and then increasing behavior. The minimum error S is reached when the value of f is 1.31 with an uncertainty of 5%. With the convergence of the error S to the level of 10^{-2} , we have determined the values of c_1 , c_2 , and f to be 1.29, 0.42, and 1.31, respectively. Consequently, the corresponding values of h_v , $k_{s,eff}$, and $k_{g,eff,||}$ are established as well and summarized in Table 7.

As shown in Table 7, when considering the two-equation model coupled with the mass and momentum equations (Eq.7) and accounting for the temperature dependency of the gas and solid thermal properties, some coefficients exhibit different values compared to their original correlations. The coefficient c_1 , which is related to the solid phase volume fraction ϵ_s , is found to increase from 0.617 to around 1.22. This value remains relatively constant across different inlet velocities. On the other hand, the coefficient c_2 , associated with gas dispersion, shows an increasing trend with higher inlet velocities and is not a constant value. This is in line with the fact that the dispersion effect increases with the

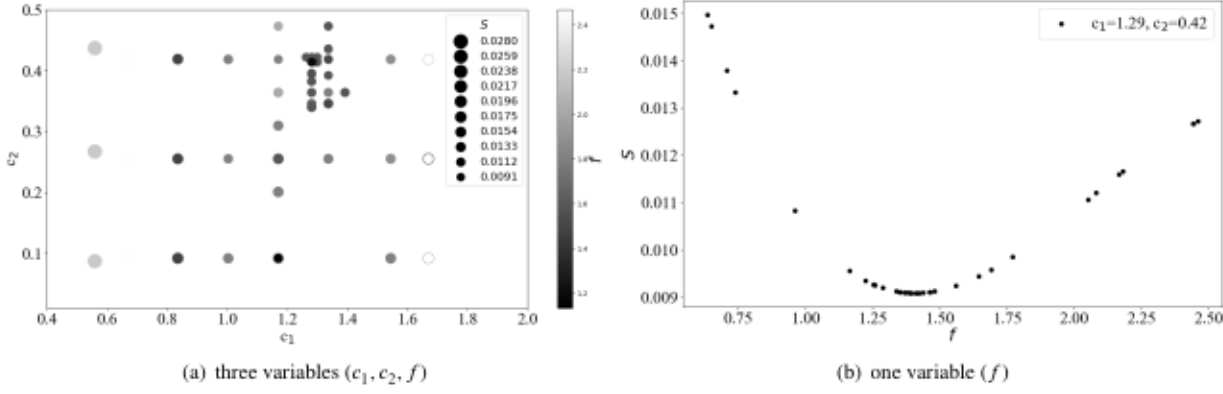


Figure 9: The influence of three variables (c_1, c_2, f) on the error S

gas velocity. Lastly, the coefficient f increases from 1.1 to around 1.5 compared to the original Wakao correlation.

Now let's revisit the comparison between the best-predicted temperature values and the measured values in Fig. 7. The solid and dashed lines represent the predicted temperature curves obtained by minimizing the error S . Taking Fig. 7 (d) as an example, the value of the error S is 9.14×10^{-3} , which is the average error across ten different locations (T_2 to T_{11}). The maximum error among these locations is 1.41×10^{-2} . For reference, the maximum temperature difference between the predicted and measured values is approximately 6.2 K. This indicates that the numerical model can accurately capture the transient temperature profiles in a packed bed with a high level of accuracy. To illustrate further the overall behavior of the packed bed, the upcoming subsection will present color maps of the simulation results.

4.1.2. Color maps of the simulation results in the full domain

In this subsection, we present a simulation result using the experimental conditions from case 1 at 4000 s. The inlet gas temperature T_g gradually increases from 292 K to 630 K within 4000 s. The inlet mass-flow rate qm is 3.56×10^{-3} kg/s, resulting in a Darcy velocity u of 0.1 m/s at room temperature. The values of c_1 , c_2 , c_3 , and f are set to 1.21, 0.11, 0, and 1.61, respectively. These values were obtained from the optimization process in the previous subsection.

Fig. 10 shows the distribution of dynamic viscosity μ_g and air density ρ_g within the packed bed region at 4000 s. The thermodynamic properties of air are updated based on the pressure and gas temperature using a linear interpolation method, utilizing the data provided in Table 5. The coupling between air density and temperature is accounted for in the mass equation in Eq. 7. At the inlet of the packed bed, the air temperature is 630 K, accompanied by a dynamic viscosity of $3.3e-5$ kg/(m · s) and a density of 0.56 kg/m³. At the outlet, the air temperature remains at room temperature, resulting in a dynamic viscosity of $1.9e-5$ kg/(m · s) and a density of 1.20 kg/m³. The dynamic viscosity of air increases by 74% over the modeled temperature range of 290 K to 630 K, while the air density experiences a decrease of 53%.

Fig. 11 presents the pressure p and Darcy velocity magnitude u fields within the packed bed region at 4000 s. The pressure at the inlet is 101358 Pa, while at the outlet, it is 101325 Pa. The significant pressure gradient observed in the packed bed region can be attributed to the inclusion of the Forchheimer equation in the model. The Darcy velocity magnitude u is 0.22 m/s at the inlet and 0.1 m/s at the outlet. The velocity is updated based on the pressure and gas temperature. Inside the packed bed, the gas velocity $\langle v_g \rangle^k$ is determined by dividing the Darcy velocity u by the porosity ϵ_g .

Fig. 12 shows the temperature fields in the packed bed region at 4000 s. The gas temperature T_g at the inlet is 630 K, while at the outlet, it is 300 K. The temperature of the gas and solid phases is updated by solving the energy equations in Eq. 7. In the packed bed region, the absolute difference between the local average gas and solid temperatures ($dT = |T_g - T_s|$) is around 4 K. The distribution of dT is influenced by the heat transfer coefficients h_v . It is worth noting that in Fig. 12 (b) there is a significant temperature difference in the upper left region. This is primarily due to the strong coupling at the interface between the gas temperature inside the packed bed and the solid temperature at the tube surface, which is much lower than the solid temperature inside the packed bed near the interface.

Fig. 13 shows the distribution of the volumetric heat transfer coefficients, h_v , within the packed bed region at 4000 s. It is worth noting that h_v is a function of space and time within the packed bed, as described by Eq. 13. The value of h_v at the inlet is 13400 (W/m³ · K) and at the outlet is 11400 (W/m³ · K). Throughout the modeled temperature range of 290–630 K, h_v experiences a decrease of 15 %, and its calculation incorporates the Wakao correlation with the factor f . The distribution of h_v aligns with the distribution of gas velocity, meaning that higher gas velocities correspond to higher h_v values. To further investigate the transient distribution of h_v within the packed bed, we plotted the values of h_v along the central axis at different times for four mass-flow rates. h_v is a function of the air density, viscosity, velocity, heat capacity, and thermal conductivity. Fig. 14 demonstrates that as the transient temperature increases, the heat transfer coefficient gradually increases as well.

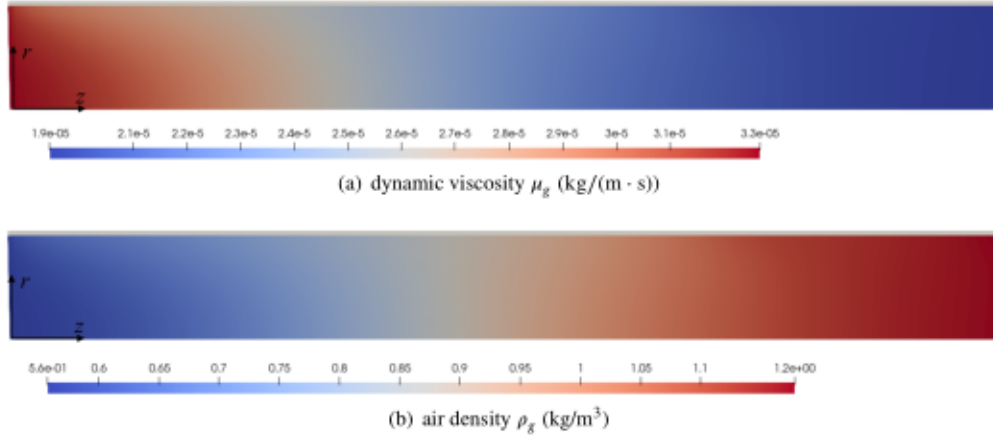


Figure 10: Dynamic viscosity and air density distribution predicted with the two-equation model.

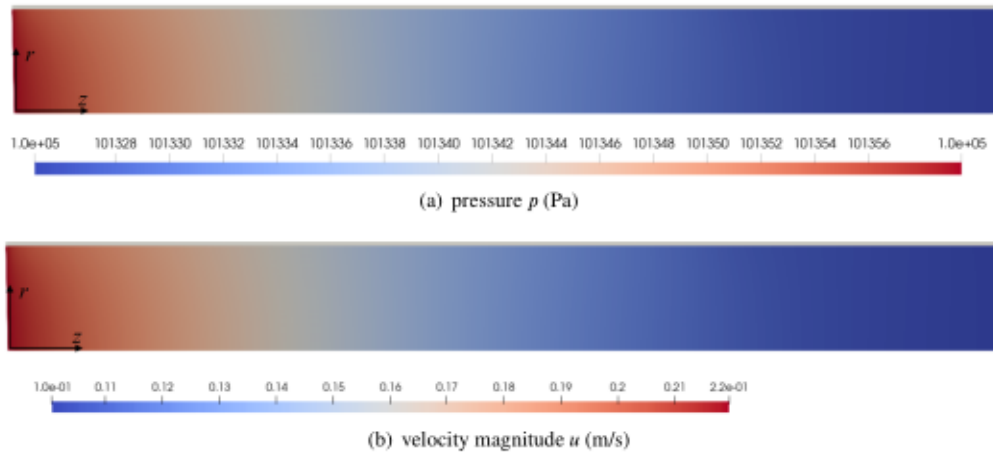


Figure 11: Pressure and velocity magnitude predicted with the two-equation model.

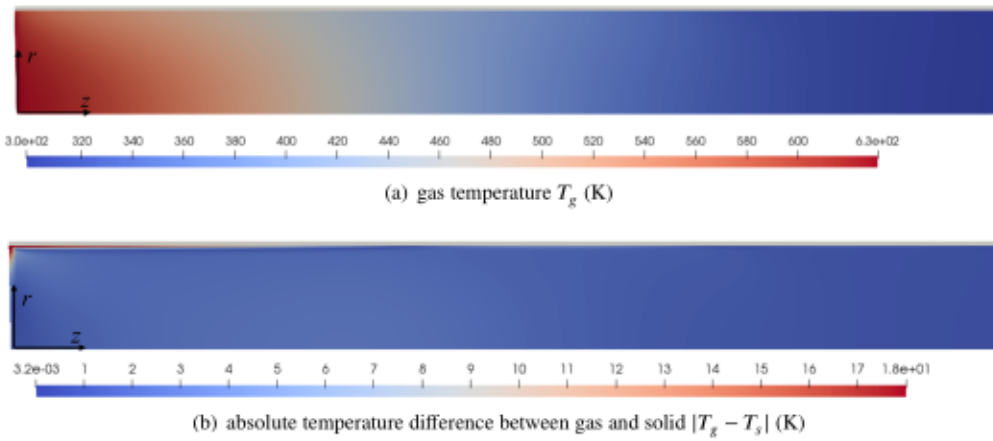


Figure 12: Gas temperature and absolute temperature difference in the porous materials region predicted with the two-equation model.

Table 7

The value of f , c_1 and c_2 obtained in the optimization process for different mass-flow rates.

qm (kg/s)	3.65×10^{-3}	5.97×10^{-3}	7.34×10^{-3}	1.02×10^{-2}
Re	58~100	100~151	150~190	223~252
c_1	1.21 ± 0.03	1.22 ± 0.03	1.27 ± 0.03	1.29 ± 0.03
c_2	0.11 ± 0.005	0.19 ± 0.008	0.28 ± 0.02	0.42 ± 0.03
f	1.61 ± 0.09	1.61 ± 0.07	1.62 ± 0.07	1.31 ± 0.09
$k_{s,eff}$ (W/(m·K))	1.1~1.6	1.1~1.5	1.1~1.4	1.2~1.4
$k_{g,eff, }$ (W/(m·K))	0.132~0.149	0.37~0.39	1.14~1.26	2.55~2.64
h_v (W/(m ³ ·K))	$1.0 \times 10^4 \sim 1.3 \times 10^4$	$1.16 \times 10^4 \sim 1.47 \times 10^4$	$1.51 \times 10^4 \sim 1.80 \times 10^4$	$1.68 \times 10^4 \sim 1.93 \times 10^4$
S	9.41×10^{-3}	9.84×10^{-3}	9.32×10^{-3}	9.14×10^{-3}

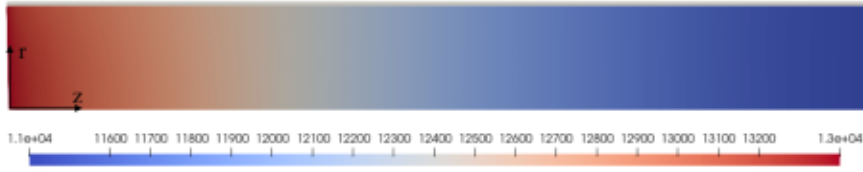


Figure 13: Volumetric heat transfer coefficient h_v (W/m³·K) distribution predicted with the two-equation model.

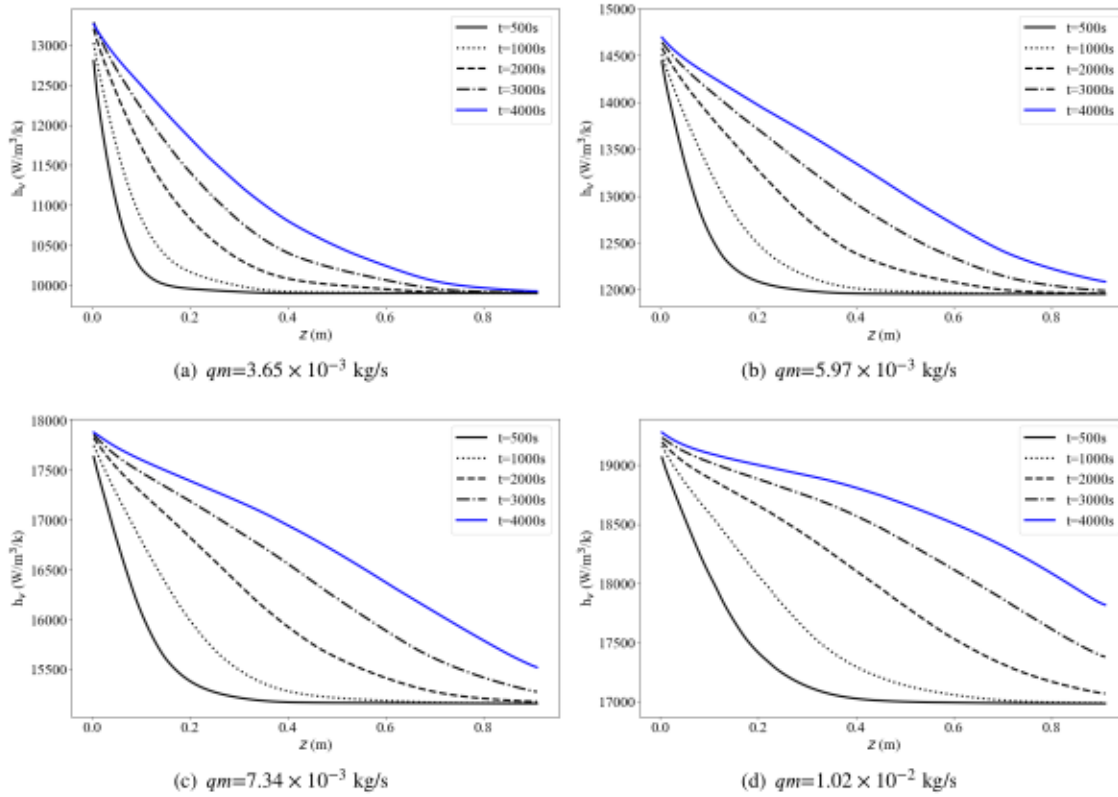


Figure 14: The distribution of h_v along the central axis with different mass flow rates.

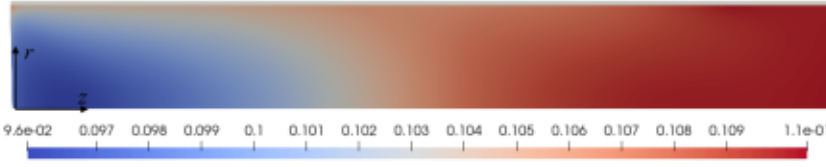
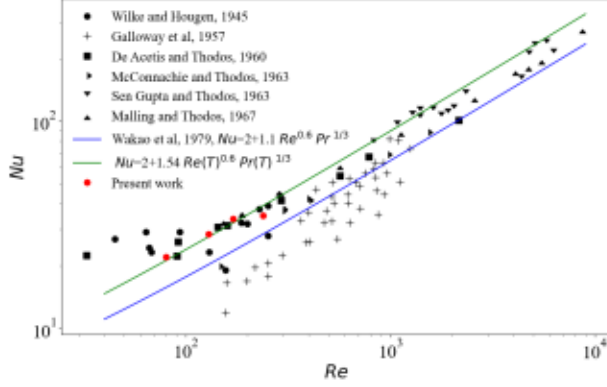
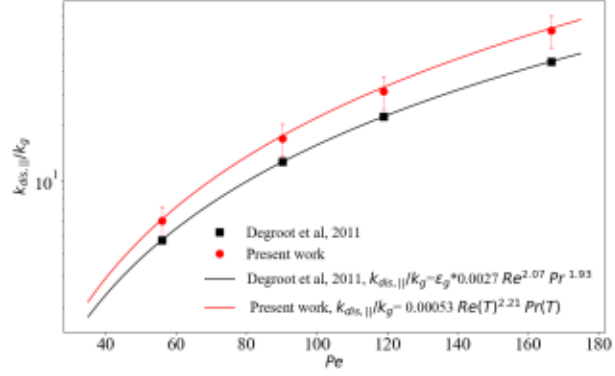


Figure 15: Biot number Bi distribution predicted with the two-equation model.



(a) Nusselt number vs. Reynolds number



(b) dispersion gas thermal conductivity vs. Peclet number

Figure 16: Comparison between the experimental data and data obtained using the numerical inverse analysis.

Fig. 15 presents Biot number Bi fields within the packed bed region at 4000 s. The Bi was determined as follows: $Bi = h_s L_c / k_s$, where $h_s = h_v \cdot d_{par} / 6(1 - \epsilon_g)$, and $L_c = V_s / A_s = d_{par} / 6$ [1]. Within the range of temperatures simulated (300–630 K), the calculated Bi values range from 0.096 to 0.11. Given that $Bi \leq 0.1$, it is justifiable to neglect the intra-particle temperature gradient. Consequently, in this study, we can reasonably assume that internal bead resistance is negligible. It should be noted that even in the presence of a thermal gradient inside the solids, Eq. 7 remains applicable. However, in that situation, h_v also considers the conduction resistance of the solid.

4.2. Comparing the heat transfer coefficient and the effective gas thermal conductivity

Heat and mass transfer in packed beds with randomized packing of particles at high temperatures is a complex phenomenon. In this study, a new correlation is developed based on the numerical inverse analysis method, taking the glass bead diameter d_{par} as the characteristic length. The dimensionless heat transfer correlation is given by:

$$Nu = 2 + 1.54 Re(T)^{0.6} Pr(T)^{1/3} \quad (16)$$

where the value of f (1.54) is obtained as the average of the four f values listed in Table 7. $Re(T)$ and $Pr(T)$ indicate that the Reynolds number (Re) and Prandtl number (Pr) are functions of temperature. Using the coefficient f and its impact on the relative error (objective function S) as an example, as shown in Fig. 9 (b), we observed that employing the new coefficients ($f = 1.54$) resulted in $S = 0.0093$. In contrast, when using the coefficients from the Wakao model ($f = 1.1$), we obtained $S = 0.01$.

In Eq. 14, S is defined as the average root mean squared relative error between measured and simulated temperatures at ten specific locations.

Fig. 16 (a) presents a comparison between heat transfer correlations reported in the work of Wakao [17] and the results obtained from the inverse analysis in this study. The correlation proposed by Wakao et al is based on a large amount of experimental data. It is obvious that the Nusselt numbers increase with increasing Reynolds numbers. As presented in Fig. 16 (a), for lower Reynolds number values ($Re = 58 \sim 252$), the data from Wilke and Hougen [60], Mallin and Thodos [61], and De Acetis and Thodos [62] are slightly above the solid blue line ($Nu = 2 + 1.1 Re^{0.6} Pr^{1/3}$). The reason for the Galloway [63] data being lower than predicted for all correlations is due to unique aspects of his study. Galloway investigated water evaporation into air from 17 mm porous spheres, arranged differently, and with solid particles maintaining constant surface temperatures. The newly proposed correlation ($Nu = 2 + 1.54 Re(T)^{0.6} Pr(T)^{1/3}$) demonstrates better suitability for the low Reynolds number range ($Re = 58 \sim 252$). It should be noted that the Reynolds number (Re) varies within the packed bed during each test, and thus the red dots in Fig. 16 (a) represent the average values of Re .

The axial gas effective thermal conductivity, $k_{g,eff}$, is expressed by Eq. 13, which is a function of both Reynolds number (Re) and Prandtl number (Pr). Table 7 demonstrates that the value of the factor c_2 is not constant but increases with increasing Re . To account for the dispersion effect resulting from the gas flow, a new correlation is developed based on the inverse analysis results obtained in this study. A previous work by DeGroot et al. [39] suggests that the commonly used characterization of dispersion based solely on the Peclet number ($Pe = Re \cdot Pr$) is not entirely accurate. In this study, we adopted a proposed function of

the form $n_1 Re^{n_2} Pr$ to account for the dispersion effect caused by the gas flow. A least-squares analysis reveals that a suitable function for the dimensionless axial dispersion conductivity can be expressed as:

$$k_{dis,||}/k_g = 0.00053 Re(T)^{2.21} Pr(T) \quad (17)$$

Fig. 16 (b) presents a comparison between the dimensionless axial dispersion conductivity $k_{dis,||}/k_g$ obtained in this study and the results of DeGroot et al. [39]. The error bars indicate that the maximum difference between the two is within 20%. It is observed that the dispersion gas thermal conductivity increases with the Peclet number, as expected from the theory presented in the introduction. In this study, the axial dispersion gas thermal conductivity is about 5.9 times and 67.1 times higher than the gas thermal conductivity when the Peclet numbers are around 55 and 165, respectively.

5. Conclusions

The objective of this work was to develop and validate a generic two-equation model coupled with mass and momentum conservation for high-temperature TES and determine the effective conductivities and the heat transfer coefficients needed to inform the two-equation model. Packed beds undergoes a transient heat storage process, resulting in a broad range of temperatures for high-temperature systems. As a consequence, the thermophysical properties of both the fluid and solid exhibit significant variations. In this work, we developed a novel packed bed TES device, based on the transient single blow technique, to investigate the effective thermal conductivity of the gas and solid phases, and the heat transfer coefficient under high-temperature operating conditions. Experiments were conducted by passing hot air through cold particles at four different mass flow rates, within a Reynolds number range of 58 to 252. Unknown parameters are simultaneously determined using numerical inverse analysis, consisting in detailed simulations and state-of-the-art multi-objective optimization. Flow inside packed beds is considered compressible and laminar; its thermal expansion is directly implemented in the mass equation by using the perfect gas law. The velocity field is modeled by the Forchheimer equation based on the Reynolds number. Heat transfer equations are described using the two-equation model in both phases inside packed beds. The variable gas and solid thermophysical properties are used over a wider range of temperatures (293K to 630K). The numerical model was implemented in finite volumes in PATO. The optimization part, which included sensitivity analysis using LHS method and the optimization process using a local optimization method (NL2SOL), was performed using the open-source optimization software Dakota. The results indicate that the value of heat transfer coefficient h_v in the two-equation model falls in the range of $1.0 \times 10^4 \sim 1.93 \times 10^4$ W/(m³ · K) under the given conditions. It was observed that the gas and solid temperatures exhibit local thermal non equilibrium within the packed bed. A new correlation has been proposed based on the Wakao correlation [17] as follows: $Nu = 2 + 1.54 Re(T)^{0.6} Pr(T)^{1/3}$. This correlation that accounts for the first time for the temperature variations of the dimensionless numbers was validated in the Reynolds number range of $Re = 58$ to 252. It was observed in this study that the dispersion gas thermal conductivity increased with increasing Peclet

number. Specifically, the axial dispersion gas thermal conductivity was found to be around 5.9 and 67.1 times higher than the gas thermal conductivity at Peclet numbers of around 55 and 165, respectively. Results for the axial dispersion gas thermal conductivity have been fitted to a new correlation: $k_{dis,||}/k_g = 0.00053 Re(T)^{2.21} Pr(T)$. The detailed high-temperature heat and mass transfer model proposed in this work was therefore validated for a large range of conditions, and new correlations were obtained to account for high-temperature effects for glass beads and air. This open perspectives towards more accurate sizing and monitoring models for high-temperature TES systems.

Declaration of Competing Interest

The authors declare that they have no known competing financial interests or personal relationships that could have appeared to influence the work reported in this paper.

Acknowledgements

This work was supported by the China Scholarship Council (CSC) program (No. 201907040064).

A. Appendix. Validation of Ergun equation

To capture the pressure drop across the packed bed, a differential pressure transmitter from EMERSON FISHER ROSEMOUNT was used, which has an uncertainty of $\pm 0.055\%$ F.S. (Full Span is 0-620 mbar). The transmitter's electrical signals were relayed to a data acquisition system for real-time observation and subsequent analysis.

The pressure drop and superficial velocity were measured for the ten mass-flow rates (qm) considered in this work. Fig. 17 compares measured results (represented by dots) with calculated results using Ergun's equation (shown as solid lines). Ergun's equation is found to accurately predict the pressure drops across the packed beds, with an R^2 value of 0.998.

B. Appendix. Optimization results at different mass flow rates

In section 4.1.1, the determination of the effective thermal conductivity of gas and solid, as well as the heat transfer coefficient, was described using a case with a high mass-flow rate ($qm=1.02 \times 10^{-2}$ kg/s). A sensitivity analysis was conducted, revealing that the coefficient c_3 , which is related to $k_{g,eff,\perp}$, had minimal impact on the output results, even at high flow rates. Next, an optimization process was performed to obtain the values of c_1 , c_2 , and f . In this appendix, we present the optimization results for three additional cases. The results are shown in Fig. 18, and the optimization process was conducted using the adaptive nonlinear least-squares algorithm (NL2SOL) in the Dakota software.

In the left side of Fig. 18, we can observe the effects of three variables, c_1 , c_2 , and f , on the error S . On the right side, the impact of a single variable, f , on the error S is presented. The optimization process initially involves determining the values of c_1 and c_2 by including all

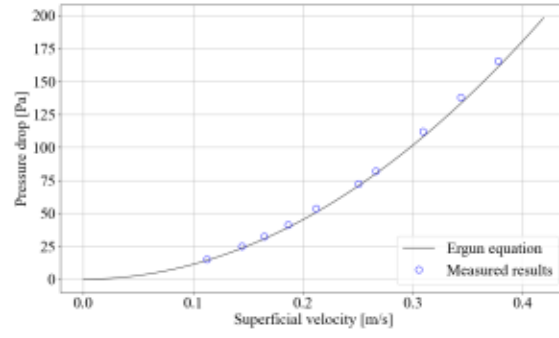


Figure 17: The comparison of measured and calculated pressure drop as a function of superficial velocity for the packed bed.

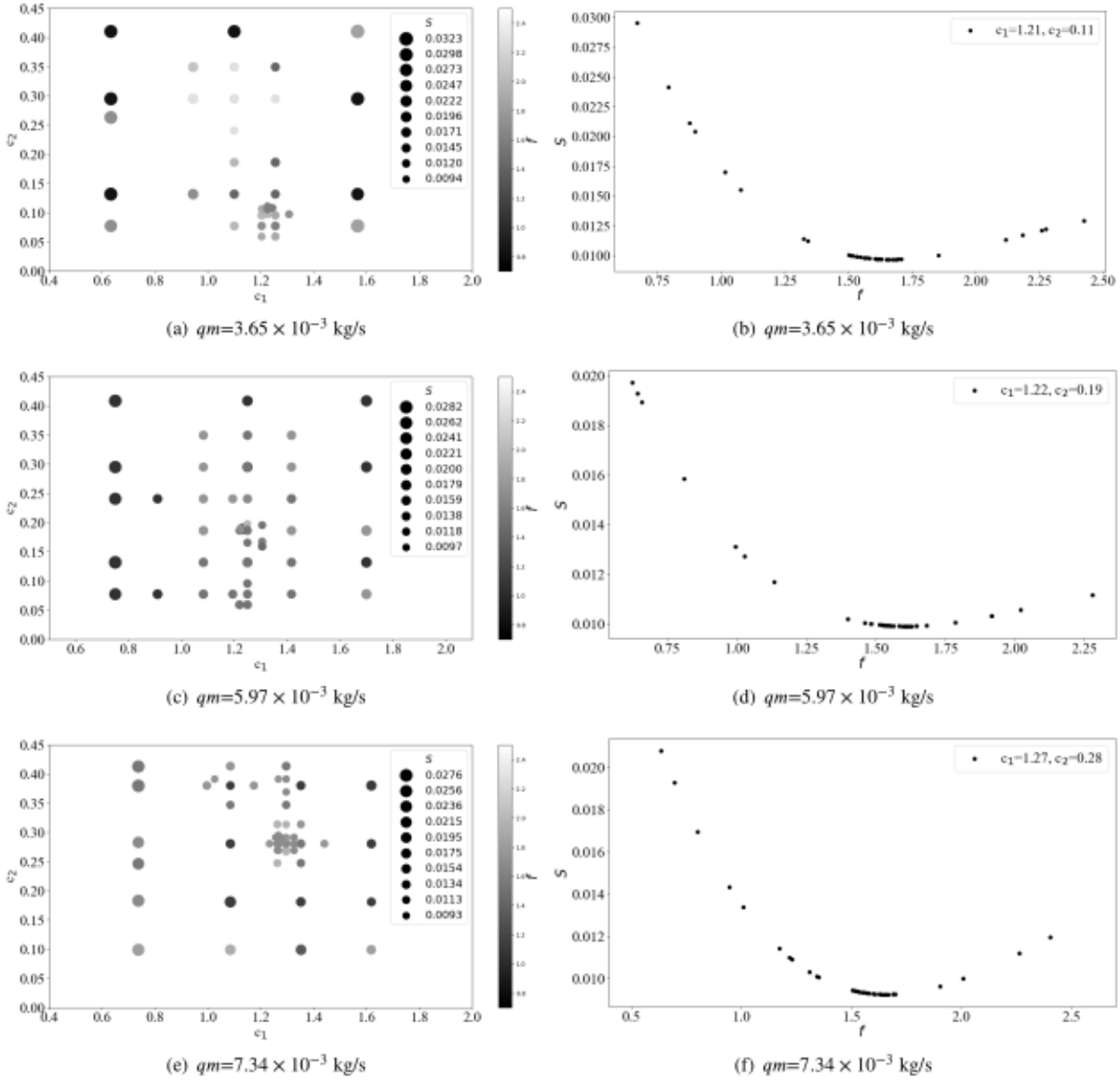


Figure 18: The influence of three variables (f, c_1, c_2) on the error S .

three variables. Then, the values of c_1 and c_2 are fixed, and the value of f is determined by introducing a single variable. Convergence ($S < 0.01$) usually takes 50 iterations with three variables, but only 25 with a single variable (f). Fig.18 (a) shows that the values of c_1 are concentrated around 1.21 and c_2 are concentrated around 0.11 when S is below 0.01, and the values of f range from 1.0 to 2.0. To further analyze the effect of f on the error, we fixed c_1 to 1.21 and c_2 to 0.11 and only varied f as the input parameter in the software. As shown in Fig.18 (b), the minimum value of the error S is achieved when the value of f is 1.61 with an uncertainty of 5%. Similarly, in the second case, the values of c_1 , c_2 , and f are 1.22, 0.19, and 1.61, respectively. In the third case, the values of c_1 , c_2 , and f are 1.27, 0.28, and 1.62, respectively. All the optimization results are summarized in Table 7.

References

- [1] T. Esence, A. Bruch, S. Molina, B. Stutz, J.-F. Fourmigué, A review on experience feedback and numerical modeling of packed-bed thermal energy storage systems, *Sol. Energy* 153 (2017) 628–654. doi:https://doi.org/10.1016/j.solener.2017.03.032.
- [2] J. Liu, L. Wang, L. Yang, L. Yue, L. Chai, Y. Sheng, H. Chen, C. Tan, Experimental study on heat storage and transfer characteristics of supercritical air in a rock bed, *Int J Heat Mass Transf* 77 (2014) 883–890. doi:https://doi.org/10.1016/j.ijheatmasstransfer.2014.06.026.
- [3] R. Anderson, S. Shiri, H. Bindra, J. F. Morris, Experimental results and modeling of energy storage and recovery in a packed bed of alumina particles, *Appl. Energy* 119 (2014) 521–529. doi:https://doi.org/10.1016/j.apenergy.2014.01.030.
- [4] K. Yang, Y. Zhang, X. Li, J. Xu, Theoretical evaluation on the impact of heat exchanger in advanced adiabatic compressed air energy storage system, *Energy Convers. Manage.* 86 (2014) 1031–1044. doi:https://doi.org/10.1016/j.enconman.2014.06.062.
- [5] H. Mozayeni, M. Negnevitsky, X. Wang, F. Cao, X. Peng, Performance study of an advanced adiabatic compressed air energy storage system, *Energy Procedia* 110 (2017) 71–76, 1st International Conference on Energy and Power, ICEP2016, 14–16 December 2016, RMIT University, Melbourne, Australia. doi:https://doi.org/10.1016/j.egypro.2017.03.108.
- [6] G. Alva, Y. Lin, G. Fang, An overview of thermal energy storage systems, *Energy* 144 (2018) 341–378. doi:https://doi.org/10.1016/j.energy.2017.12.037.
- [7] E. Oró, A. de Gracia, A. Castell, M. Farid, L. Cabeza, Review on phase change materials (pcms) for cold thermal energy storage applications, *Appl. Energy* 99 (2012) 513–533. doi:https://doi.org/10.1016/j.apenergy.2012.03.058.
- [8] F. Agyenim, N. Hewitt, P. Eames, M. Smyth, A review of materials, heat transfer and phase change problem formulation for latent heat thermal energy storage systems (lhtess), *Renewable Sustainable Energy Rev.* 14 (2) (2010) 615–628. doi:https://doi.org/10.1016/j.rser.2009.10.015.
- [9] A. Gil, M. Medrano, I. Martorell, A. Lázaro, P. Dolado, B. Zalba, L. F. Cabeza, State of the art on high temperature thermal energy storage for power generation. part I—concepts, materials and modelization, *Renewable Sustainable Energy Rev.* 14 (1) (2010) 31–55. doi:https://doi.org/10.1016/j.rser.2009.07.035.
- [10] X. Yang, Z. Lu, Q. Bai, Q. Zhang, L. Jin, J. Yan, Thermal performance of a shell-and-tube latent heat thermal energy storage unit: Role of annular fins, *Appl. Energy* 202 (2017) 558–570. doi:https://doi.org/10.1016/j.apenergy.2017.05.007.
- [11] B. Xu, P.-W. Li, C. L. Chan, Extending the validity of lumped capacitance method for large biot number in thermal storage application, *Sol. Energy* 86 (6) (2012) 1709–1724. doi:https://doi.org/10.1016/j.solener.2012.03.016.
- [12] M. Hänchen, S. Brückner, A. Steinfeld, High-temperature thermal storage using a packed bed of rocks – heat transfer analysis and experimental validation, *Appl. Therm. Eng.* 31 (10) (2011) 1798–1806. doi:https://doi.org/10.1016/j.applthermaleng.2010.10.034.
- [13] Y. Qu, L. Wang, X. Lin, H. Ling, Y. Bai, S. Zhang, H. Chen, Heat transfer characteristics of mixed convection in packed beds, *Chem. Eng. Sci.* 255 (2022) 117679. doi:https://doi.org/10.1016/j.ces.2022.117679.
- [14] T. Schumann, Heat transfer: A liquid flowing through a porous prism, *J. Franklin Inst.* 208 (3) (1929) 405–416. doi:https://doi.org/10.1016/S0016-0032(29)91186-8.
- [15] B. Pomeroy, Thermal energy storage in a packed bed of iron spheres with liquid sodium coolant, *Sol. Energy* 23 (6) (1979) 513–515. doi:https://doi.org/10.1016/0038-092X(79)90075-6.
- [16] A. Saez, B. McCoy, Dynamic response of a packed bed thermal storage system—a model for solar air heating, *Sol. Energy* 29 (3) (1982) 201–206. doi:https://doi.org/10.1016/0038-092X(82)90206-7.
- [17] N. Wakao, S. Kaguei, T. Funazkri, Effect of fluid dispersion coefficients on particle-to-fluid heat transfer coefficients in packed beds: Correlation of nusselt numbers, *Chem. Eng. Sci.* 34 (3) (1979) 325–336. doi:https://doi.org/10.1016/0009-2509(79)85064-2.
- [18] G. Zanganeh, A. Pedretti, S. Zavattoni, M. Barbato, A. Steinfeld, Packed-bed thermal storage for concentrated solar power – pilot-scale demonstration and industrial-scale design, *Sol. Energy* 86 (10) (2012) 3084–3098. doi:https://doi.org/10.1016/j.solener.2012.07.019.
- [19] G. Zanganeh, A. Pedretti, A. Haselbacher, A. Steinfeld, Design of packed bed thermal energy storage systems for high-temperature industrial process heat, *Appl. Energy* 137 (2015) 812–822. doi:https://doi.org/10.1016/j.apenergy.2014.07.110.
- [20] R. Anderson, L. Bates, E. Johnson, J. F. Morris, Packed bed thermal energy storage: A simplified experimentally validated model, *J. Energy Storage* 4 (2015) 14–23. doi:https://doi.org/10.1016/j.est.2015.08.007.

- [21] S. Pati, A. Borah, M. P. Boruah, P. R. Randive, Critical review on local thermal equilibrium and local thermal non-equilibrium approaches for the analysis of forced convective flow through porous media, *Int. Commun. Heat Mass Transf.* 132 (2022) 105889. doi:<https://doi.org/10.1016/j.icheatmasstransfer.2022.105889>.
- [22] M. Quintard, Introduction to heat and mass transport in porous media, Porous Media Interaction with High Temperature and High Speed Flows, Von Karman Institute for Fluid Dynamics, Rhode Saint Genese, Belgium (2015).
- [23] X. Ma, C. Fan, W. Shao, Q. Cao, Z. Cui, Numerical and experimental studies of packed bed thermal energy storage system based on a novel transient energy model, *Energy Sci. Eng.* 11 (2) (2023) 727–744. doi:<https://doi.org/10.1002/ese3.1358>.
- [24] J. Lachaud, J. Scoggins, T. Magin, M. Meyer, N. Mansour, A generic local thermal equilibrium model for porous reactive materials submitted to high temperatures, *Int J Heat Mass Transf.* 108 (2017) 1406–1417. doi:<https://doi.org/10.1016/j.ijheatmasstransfer.2016.11.067>.
- [25] M. Quintard, M. Kaviany, S. Whitaker, Two-medium treatment of heat transfer in porous media: numerical results for effective properties, *Adv. Water Resour.* 20 (2) (1997) 77–94. doi:[https://doi.org/10.1016/S0309-1708\(96\)00024-3](https://doi.org/10.1016/S0309-1708(96)00024-3).
- [26] S. Liu, A. Ahmadi-Senichault, C. Levat, J. Lachaud, Experimental investigation on the validity of the local thermal equilibrium assumption in ablative-material response models, *Aerosp. Sci. Technol.* (2023) 108516doi:<https://doi.org/10.1016/j.ast.2023.108516>.
- [27] N. Wakao, S. Kaguci, Heat and mass transfer in packed bedsgordon and breach science publications, New York (1982).
- [28] W. Ranz, Friction and transfer coefficients for single particles and packed beds, *Chem. Eng. Prog.* 48 (1952) 247–253.
- [29] T. Galloway, B. Sage, A model of the mechanism of transport in packed, distended, and fluidized beds, *Chem. Eng. Sci.* 25 (3) (1970) 495–516. doi:[https://doi.org/10.1016/0009-2509\(70\)80048-3](https://doi.org/10.1016/0009-2509(70)80048-3).
- [30] J. Yang, J. Wang, S. Bu, M. Zeng, Q. Wang, A. Nakayama, Experimental analysis of forced convective heat transfer in novel structured packed beds of particles, *Chem. Eng. Sci.* 71 (2012) 126–137. doi:<https://doi.org/10.1016/j.ces.2011.12.005>.
- [31] M. Naghash, F. Fathieh, R. W. Besant, R. W. Evitts, C. J. Simonson, Measurement of convective heat transfer coefficients in a randomly packed bed of silica gel particles using ihtp analysis, *Appl. Therm. Eng.* 106 (2016) 361–370. doi:<https://doi.org/10.1016/j.applthermaleng.2016.06.027>.
- [32] M. Nazari, D. Jalali Vahid, R. K. Saray, Y. Mahmoudi, Experimental investigation of heat transfer and second law analysis in a pebble bed channel with internal heat generation, *Int J Heat Mass Transf.* 114 (2017) 688–702. doi:<https://doi.org/10.1016/j.ijheatmasstransfer.2017.06.079>.
- [33] V. Sassanis, L. Gamet, M. Rolland, R. Ma, V. Pozzobon, Numerical determination of the volumetric heat transfer coefficient in fixed beds of wood chips, *Chem. Eng. J.* 417 (2021) 128009. doi:<https://doi.org/10.1016/j.cej.2020.128009>.
- [34] F. Augier, F. Idoux, J. Delenne, Numerical simulations of transfer and transport properties inside packed beds of spherical particles, *Chem. Eng. Sci.* 65 (3) (2010) 1055–1064. doi:<https://doi.org/10.1016/j.ces.2009.09.059>.
- [35] H. Scandelli, Modélisation multi-échelle des milieux poreux réactifs à haute température appliquée aux protections thermique spatiale et à la pyrolyse de la biomasse., Theses, HESAM Université (Oct. 2022). URL <https://pastel.archives-ouvertes.fr/tel-04042460>
- [36] J. Petrasch, F. Meier, H. Friess, A. Steinfeld, Tomography based determination of permeability, dupuit-forchheimer coefficient, and interfacial heat transfer coefficient in reticulate porous ceramics, *Int. J. Heat Fluid Flow* 29 (1) (2008) 315–326. doi:<https://doi.org/10.1016/j.ijheatfluidflow.2007.09.001>.
- [37] A. A. Jalalzadeh-Azar, W. G. Steele, G. A. Adebisi, Heat Transfer in a High-Temperature Packed Bed Thermal Energy Storage System—Roles of Radiation and Intraparticle Conduction, *J. Energy Res. Technol.* 118 (1) (1996) 50–57. doi:<https://doi.org/10.1115/1.2792693>.
- [38] M. Cascetta, G. Cau, P. Puddu, F. Serra, A comparison between cfd simulation and experimental investigation of a packed-bed thermal energy storage system, *Appl. Therm. Eng.* 98 (2016) 1263–1272. doi:<https://doi.org/10.1016/j.applthermaleng.2016.01.019>.
- [39] C. T. DeGroot, A. G. Straatman, Closure of non-equilibrium volume-averaged energy equations in high-conductivity porous media, *Int J Heat Mass Transf.* 54 (23) (2011) 5039–5048. doi:<https://doi.org/10.1016/j.ijheatmasstransfer.2011.07.018>.
- [40] C. Yang, A. Nakayama, A synthesis of tortuosity and dispersion in effective thermal conductivity of porous media, *Int. J. Heat Mass Transfer.* 53 (15) (2010) 3222–3230. doi:<https://doi.org/10.1016/j.ijheatmasstransfer.2010.03.004>.
- [41] A. J. van Eckelen, J. Lachaud, Numerical validation of an effective radiation heat transfer model for fiber preforms, *Journal of Spacecraft and Rockets* 48 (3) (2011) 534–537. doi:10.2514/1.51865.
- [42] Z. Abdulagatova, I. Abdulagatov, V. Emirov, Effect of temperature and pressure on the thermal conductivity of sandstone, *Int. J. Rock Mech. Min. Sci.* 46 (6) (2009) 1055–1071. doi:<https://doi.org/10.1016/j.ijrmms.2009.04.011>.
- [43] X. lin Xia, X. Chen, C. Sun, Z. huan Li, B. Liu, Experiment on the convective heat transfer from airflow to skeleton in open-cell porous foams, *Int J Heat Mass Transf.* 106 (2017) 83–90. doi:<https://doi.org/10.1016/j.ijheatmasstransfer.2016.10.053>.

- [44] W. van Antwerpen, C. du Toit, P. Rousseau, A review of correlations to model the packing structure and effective thermal conductivity in packed beds of mono-sized spherical particles, *Nucl. Eng. Des.* 240 (7) (2010) 1803–1818. doi:<https://doi.org/10.1016/j.nucengdes.2010.03.009>.
- [45] D. Okello, O. J. Nydal, E. J. Banda, Experimental investigation of thermal de-stratification in rock bed tes systems for high temperature applications, *Energy Convers. Manage.* 86 (2014) 125–131. doi:<https://doi.org/10.1016/j.enconman.2014.05.005>.
- [46] A. Shitzer, M. Levy, Transient Behavior of a Rock-Bed Thermal Storage System Subjected to Variable Inlet Air Temperatures: Analysis and Experimentation, *J. Sol. Energy Eng.* 105 (2) (1983) 200–206. doi:[10.1115/1.3266366](https://doi.org/10.1115/1.3266366).
- [47] S. S. Halkarni, A. Sridharan, S. Prabhu, Estimation of volumetric heat transfer coefficient in randomly packed beds of uniform sized spheres with water as working medium, *Int. J. Therm. Sci.* 110 (2016) 340–355. doi:<https://doi.org/10.1016/j.ijthermalsci.2016.07.012>.
- [48] G. E. Mueller, Radial void fraction distributions in randomly packed fixed beds of uniformly sized spheres in cylindrical containers, *Powder Technol.* 72 (3) (1992) 269–275. doi:[https://doi.org/10.1016/0032-5910\(92\)80045-X](https://doi.org/10.1016/0032-5910(92)80045-X).
- [49] W. Sobieski, A. Trykozko, Darcy's and forchheimer's laws in practice. part 1. the experiment, Technical Sciences/University of Warmia and Mazury in Olsztyn (2014).
- [50] A. Montillet, Flow Through a Finite Packed Bed of Spheres: A Note on the Limit of Applicability of the Forchheimer-Type Equation, *J. Fluids Eng.* 126 (1) (2004) 139–143. doi:[10.1115/1.1637928](https://doi.org/10.1115/1.1637928).
- [51] A. M. Amao, Mathematical model for darcy forchheimer flow with applications to well performance analysis, Ph.D. thesis (2007).
- [52] J. C. Chen, S. W. Churchill, Radiant heat transfer in packed beds, *AIChE Journal* 9 (1) (1963) 35–41.
- [53] J. Lachaud, N. N. Mansour, Porous-material analysis toolbox based on openfoam and applications, *J. Thermophys Heat Transfer* 28 (2) (2014) 191–202. doi:[10.2514/1.T4262](https://doi.org/10.2514/1.T4262).
- [54] B. J. McBride, S. Gordon, M. A. Reno, Thermodynamic Data for Fifty Reference Elements, NASA TP-3287-REV1, Glenn Research Center, Cleveland, Ohio (February 2001).
- [55] M. Pertermann, A. G. Whittington, A. M. Hofmeister, F. J. Spera, J. Zayak, Transport properties of low-sanidine single-crystals, glasses and melts at high temperature, *Contrib. Mineral. Petrol.* 155 (6) (2008) 689–702. doi:<https://doi.org/10.1007/s00410-007-0265-x>.
- [56] B. Adams, W. Bohnhoff, K. Dalbey, M. Ebeida, J. Eddy, M. Eldred, R. Hooper, P. Hough, K. Hu, J. Jakeman, et al., Dakota, a multi-level parallel object-oriented framework for design optimization, parameter estimation, uncertainty quantification, and sensitivity analysis: Version 6.13 user's manual., Tech. rep., Sandia National Lab.(SNL-NM), Albuquerque, NM (United States) (2020).
- [57] A. Olsson, G. Sandberg, O. Dahlblom, On latin hypercube sampling for structural reliability analysis, *Struct. Saf.* 25 (1) (2003) 47–68. doi:[https://doi.org/10.1016/S0167-4730\(02\)00039-5](https://doi.org/10.1016/S0167-4730(02)00039-5).
- [58] J. E. Dennis Jr, D. M. Gay, R. E. Walsh, An adaptive nonlinear least-squares algorithm, *ACM Trans. Math. Software* 7 (3) (1981) 348–368.
- [59] J. C. Helton, F. J. Davis, Sampling-based methods for uncertainty and sensitivity analysis, Tech. rep., Sandia National Lab.(SNL-NM), Albuquerque, NM (United States); Sandia ... (2000).
- [60] C. R. Wilke, O. Hougen, Mass transfer in the flow of gases through granular solids extended to low modified reynolds numbers, *Trans. Am. Inst. Chem. Eng* 41 (4) (1945) 445–451.
- [61] G. Mallin, G. Thodos, Analogy between mass and heat transfer in beds of spheres: Contributions due to end effects, *Int J Heat Mass Transf* 10 (4) (1967) 489–498. doi:[https://doi.org/10.1016/0017-9310\(67\)90169-X](https://doi.org/10.1016/0017-9310(67)90169-X).
- [62] J. D. Acetis, G. Thodos, Mass and heat transfer in flow of gases through spherical packings, *Industrial & Engineering Chemistry* 52 (12) (1960) 1003–1006. doi:[10.1021/ie50612a026](https://doi.org/10.1021/ie50612a026).
- [63] L. Galloway, W. Komarnicky, N. Epstein, Effect of configuration on mass and heat transfer in beds stacked spheres, *Can. J. Chem. Eng* 135 (1957) 139–150.